

The Annulus-Filtered E and B Modes in CMBR Polarization

Tzihong Chiueh and Cheng-Jiun Ma

Physics Department, National Taiwan University, Taipei, Taiwan

Institute of Astronomy and Astrophysics, Academia Sinica, Taipei, Taiwan

Received _____; accepted _____

submitted to ApJ

ABSTRACT

Although it has previously been recognized that the CMB polarization measurement on a sky ring is able to separate the B and E -mode patterns, we show that the rotational symmetry of the CMB polarization measurement is indeed unique, in that it enables the B and E modes to be separately measured in a simple and clean manner. The separation of B and E modes can in principle be achieved even with a single-polarization detector of arbitrary beam pattern. Based on this premise, a specific observing strategy is suggested, where the telescope scans along a sky circle with the polarimeter axis always oriented to a fixed direction with respect to the radial direction of the sky circle. The observational strategy for B -mode measurements can further be refined by choosing appropriate beam sizes to suppress the accidental E -mode leakage. We present the expected variances of the measured E and B -mode surface-brightness fluctuations as functions of the sky annulus radius and beam size. The measured peak power is expected to be up to 10% of the total power contained in the CMB polarization fluctuations for both B and E modes. The temperature-polarization, or $T - E$, correlation can be measured by the present method as well. By adopting this strategy, the AMiBA experiment is expected to detect, in a single sky annulus, a 1σ B -mode signal in 340 hours.

Subject headings: cosmology; cosmic microwave background — polarization

1. Introduction

The CMB anisotropy provides direct information of the oldest relics of large-scale structures left from the Big-Bang. These CMB photons generally contain two kinds of

information at every frequency band, the intensity and the polarization. Though the CMB photons are originated at the last scattering surface near red-shift $z \sim 1000$, they can be re-processed along the light paths before reaching us, notably by the gravitational and Doppler effects. These effects dominantly affect the photon intensity, or the temperature anisotropy; they can also affect the photon polarization, but only to a much lesser degree. Thus, unlike the temperature anisotropy, it is believed that the CMB polarization is a sensitive probe to the universe at a specific epoch when the photon temperature is about 3000 degrees and the photon optical depth τ about 1/2. The CMB polarization is generated at this optical depth through the Thomson scattering of the pre-existing temperature anisotropy by a background of homogeneous free electrons(Rees 1968; Bond and Efstathiou 1984; Polnarev 1985).

Different normal modes in the primordial fluctuations yield different characteristics in the temperature anisotropy, thereby yielding different types of polarization patterns. It has been pointed out that these different polarization patterns can be divided into two classes: the electric-type (E) pattern and the magnetic-type (B) pattern(Kamionkowsky et al. 1997; Zaldarriaga and Seljak 1997; Hu and White 1997). The primordial density perturbations (scalar modes) generate only the E pattern, but the B pattern can only be generated by the primordial gravitational waves (tensor modes) and vortex motion (vector modes). Since different patterns were originated from different physics, the ability to separate the E and B patterns cleanly has become a measure of success for CMB polarization experiments in a foreseeable future.

Following the conventional approach to temperature anisotropy, most past works that addressed the CMB polarization tended to focus on how the two kinds of polarization patterns may be separated in the Fourier domain. Such an approach is natural for the wide-sky maps, such as those planned for the MAP and Planck missions. However, for the ground-based and balloon-borne experiments, the wide-sky maps are

impossible to obtain, and the adopted strategy is often deep exposure of a small-patch of sky(Staggs et al. 1999; White et al. 1999; Lo et al. 2000). Unlike the wide-sky map, the local maps cannot naturally satisfy the periodic boundary conditions, and hence a brute-force Fourier analysis to extract the power spectrum can often introduce distortion to the original data and produces un-desirable effects. The problem is particularly acute for the B -mode measurement due to the small B -mode signals. For this reason, the real-space analysis of local maps has been called for(Seljak and Zaldarriaga 1998; Zaldarriaga 1998; Chiueh 2000; Chiueh & Ma 2000; Tegmark and de Oliveria-Costa 2000).

In the past years, an alternative approach has also been examined in an attempt to alleviating the problem of boundary conditions(Zaldarriaga 1998; Revenu et al. 2000). When the measurements are taken along a ring on the sky, the data will automatically satisfy the periodic boundary condition with discrete wavenumbers. As the ring diameter can be over tens of degrees, the large sky coverage of the ring permits one to extract a wide spectrum of discrete modes from the measurement. Though this approach solves the problem of boundary conditions, the separation of B and E modes is still not natural, as it requires precise short-term calibration of detectors within the individual ring(O'Dell et al 2000) and long-term calibration across different rings(Revenu et al. 2000) in order to extract the appropriate Stokes Q and U to construct E and B modes.

Recently, it has been proposed that with a suitable projection of the real-space data, one is able to separate the E and B patterns directly from the local map without resorting to the Fourier analysis(Chiueh 2000; Chiueh & Ma 2000). They also illustrate what the visual appearances of the unfamiliar E and B tensor patterns are in the projected vector space. In these previous works, the polarization tensor is first projected into a vector and a pseudo-vector field through differentiation of the measured data, and these vector fields are further projected into a scalar and a pseudo-scalar through a contour integration of

arbitrary shape. The scalar component results from the E mode and the pseudo-scalar from the B mode.

Though illuminating, this proposed projection, however, suffers from a differential operation on the data for projecting the polarization tensors into vectors, which invariably amplifies the measurement noises. Despite that the differentiation is followed by a contour integration to construct the projected E and B scalars, which damps out the amplified noises, the noise damping can hardly compensate for the noise amplification. Hence it is desirable to pursue a different method that can also cleanly separate the B and E patterns in the real space.

A tensor (vector) can be projected into a vector (scalar) through a vector operation, which can either be a projection-derivative or a projection-integration along a given contour. Both have been used in our previous proposal(Chiueh 2000; Chiueh & Ma 2000). As the differentiation amplifies the data noise, the former is ruled out. For the latter, various projection integrations are available. As will be shown in this paper, the only viable ones, useful for separating the pseudo-tensor patterns from the tensor pattern are those that assume circular integration contours. It has been pointed out that circular-scan observations allow the E and B modes to be separated(Zaldarriaga 1998). The present work reinforces this observation and shows that the scanning observation along circles is indeed the only one strategy that permits the B and E modes to be cleanly separated without involving data differencing.

This result is particularly relevant for the scanning observations conventionally conducted by, for example, balloon-borne and ground-based experiments. The recommended circular scanning observation is nothing but integration of data along a given sky circle over a long period of time without distinguishing variations on the circle. This is to be contrasted to integration along a sky contour of arbitrary shape proposed by

(Chiueh 2000), and contrasted to extraction of discrete modes on a sky circle analyzed by (Zaldarriaga 1998). In fact, to achieve the goal of separating E and B modes, it is also necessary that the polarimeter axis of the detector also rotates as the telescope sweeps along the sky circle. Be precise, the polarimeter axis must always orient toward a fixed direction with respect to the local radial direction of the sky circle. The AMiBA telescope can have this capability(Lo et al. 2000). We will assess how AMiBA is expected to perform using this observational strategy.

This paper is organized as follows. Sec.(2) gives the formulation, with which the constraint on the shape of the integration contour is derived. The implications for the projection integrals with circular contours are examined in Sec.(3). Sec.(4) addresses the measurement of the E modes using this method. Sec.(5) discusses the measurement strategy for the much weaker B modes. Correlation of E -mode polarization with temperature anisotropy is addressed in Sec.(6). In Sec.(7), we study how a finite beam width can affect the sharp-beam cases considered in the previous sections, and show that the ability of the circular-scan strategy for separating B modes from E modes can be much improved via a finite-size beam. Discussions on the AMiBA performance are given in Sec.(8). Conclusions are given in Sec.(9). Throughout this paper, we adopt the flat-sky approximation since the CMB fluctuations of interest are at most few degrees in size.

2. Projection Contour Integral

The polarization tensor \mathbf{P} can be expressed as(Chiueh 2000)

$$\begin{aligned} \mathbf{P} &= Q\sigma_x + U\sigma_y = [\nabla\nabla - (\hat{z} \times \nabla)(\hat{z} \times \nabla)]f + [\nabla(\hat{z} \times \nabla) + (\hat{z} \times \nabla)\nabla]g \\ &= Q + iU = 4\frac{\partial^2}{\partial\bar{w}^2}(f + ig) \end{aligned} \quad (1)$$

where σ_x and σ_y are the "3" and "1" components of the Pauli matrices, respectively, and f and g are real functions denoting the E and B components, respectively. Moreover, from the third equality on, we have used a complex representation for \mathbf{P} , where $w = x + iy$ and $\bar{w} = x - iy$. A convenient way to construct a scalar from \mathbf{P} proceeds as follows. Pick a closed contour C on the polarization field, contract the tensor \mathbf{P} with a suitable local tensor to form a scalar/pseudo-scalar at every point on the contour, and then sum up these scalar quantities over the contour to obtain a contour-integrated value. Mathematically, the operation can be written as

$$Y \equiv 4 \int_C \frac{\partial^2(f + ig)}{\partial \bar{w}^2} \bar{w} d\bar{w}. \quad (2)$$

where $\bar{w} d\bar{w}$ is the local tensor for projecting out the scalar Y , C is the closed contour along which the line integration is performed, and the coordinate \bar{w} can be chosen so that the origin is inside the contour. In terms of the Stokes Q and U , Eq.(2) is

$$Y = \int_C [(xQ + yU)dx - (yQ - xU)dy] - i \int_C [(yQ - xU)dx + (xQ + yU)dy]. \quad (3)$$

Considering the fact that $\bar{w} \partial^2 A / \partial \bar{w}^2$ can be expressed as a total derivative, equal to $\partial[\bar{w}(\partial A / \partial \bar{w}) - A] / \partial \bar{w}$, and that f and g are both analytical functions, we arrive at the following expression for Y of Eq.(2),

$$Y = i \int_C \left[\frac{\partial F}{\partial y} dx - \frac{\partial F}{\partial x} dy \right], \quad (4)$$

where $F \equiv \bar{w}(\partial(f + ig) / \partial \bar{w}) - (f + ig)$. Using the Stokes theorem and the fact that $\nabla^2 = 4\partial^2 / \partial \bar{w} \partial w$, Eq.(4) can further be rewritten as

$$Y = -i \int \nabla^2 F d^2 S = -i \int \bar{w} \frac{\partial}{\partial \bar{w}} \nabla^2(f + ig) d^2 S, \quad (5)$$

where the surface integration is confined within the area bounded by the contour C . Instead of placing an integration limit for the surface integral, we may multiply the integrand of Eq.(5) by a top-hat filter function $W(x, y)$ and carry out the surface integral without

an explicit bound, where $W(x, y) = 1$ inside the contour C and $W(x, y) = 0$ otherwise. This permits a convenient way to evaluate the second equality of Eq.(5). Note that $\bar{w}\partial/\partial\bar{w} = (\partial/\partial\ln r) + i(\partial/\partial\phi)$ in the polar coordinate. With an integration by part, Eq.(5) becomes

$$Y = i \int \left[\frac{\partial W}{\partial \ln r} + 2W + i \frac{\partial W}{\partial \phi} \right] \nabla^2(f + ig) r dr d\phi. \quad (6)$$

Note that W is a real quantity, and both real and imaginary parts of Y generally contain a mixture of the real E -mode f and real B -mode g . However, at some special arrangements, E and B modes can become separated, with g contributing only to the real part and f only to the imaginary part, or the opposite. These situations only happen when r^2W depends either on r or on ϕ , but not on both. The choice of depending only on ϕ can be ruled out since such a window function is not compact. Thus, the one and only one choice for the contour must be such that $W(x, y) = W(r)$, and moreover $W(r) = \Theta(R - r)$, a circular top-hat filter function of radius R .

That is, the only scanning trajectory that is capable of projecting out the desired scalar and pseudo-scalar is when it is a circle. The circular scan yields the real part of Y to be entirely contributed by the B mode and the imaginary part of Y by the E mode. It also leaves Y to depend on a single parameter, i.e., the radius R of the circle. The above derivation also proves that a special case of circular-scan observations analyzed by Zaldarriaga (Zaldarriaga 1998) is indeed a unique one.

3. *E-B* Amplitude through a Circular Filter

We now examine what quantities of the polarization tensor \mathbf{P} are to be extracted from the projection integration along a circle. It will also be shown that the projection of \mathbf{P} defined in Eq.(2) corresponds to physical rotation of the polarimeter axes, so that they remain fixed with respect to the local radial direction along the circle.

Let the circular contour of radius R center at \mathbf{x}_0 , so that $r \equiv |\mathbf{x} - \mathbf{x}_0|$. It then follows from Eqs.(3) that

$$\begin{aligned} Y(R; \mathbf{x}_0) &= -iR^2 \int_0^{2\pi} [(\cos(2\phi)Q + \sin(2\phi)U) + i(\cos(2\phi)U - \sin(2\phi)Q)] d\phi \\ &= -iR^2 \int_0^{2\pi} [r \frac{\partial}{\partial r} (\frac{1}{r} \frac{\partial}{\partial r}) - \frac{1}{r^2} \frac{\partial^2}{\partial \phi^2} + \frac{2i}{r} \frac{\partial}{\partial \phi} (\frac{\partial}{\partial r} - \frac{1}{2r})] (f + ig) d\phi \\ &= i \int_0^{2\pi} \int_0^\infty \bar{W}(r) \nabla^2 (f(\mathbf{x}) + ig(\mathbf{x})) r dr d\phi, \end{aligned} \quad (7)$$

where the second equality can be straightforwardly derived from Eq.(2) and the third equality is simply Eq.(6) with a filter function $\bar{W} \equiv (1/r) d(r^2 W) / dr$. Similar expressions for Eq.(7) have also been derived before (Seljak and Zaldarriaga 1998; Crittenden et al. 2000) based on a related idea in weak lensing studies (Kaiser et al. 1994).

The angular factors on the right of the first equality in Eq.(7) are the familiar ones. It describes how Q and U rotate as the second-rank tensor components when the coordinate rotates. In fact, these angular factors mean that the polarization tensor $Q + iU$ must be rotated to $Q_0 + iU_0$ of a preferred coordinate (x_0, y_0) , where the x_0 -direction is along the local radial direction of the sky circle and the y_0 -direction along the local azimuthal direction. This point is central to the present work, in that not only the scanning trajectory should be a circle, but the polarimeter axes of the telescope must rotate as well.

The separation of E and B modes depends critically on a perfect angular integration and perfect polarimeter-axis alignment. The quantity Y thus measures the angular average of $4r^2(\partial^2 f / \partial(r^2)^2)$ of the E mode and $4r^2(\partial^2 g / \partial(r^2)^2)$ of the B mode. It turns out that these unfamiliar derivatives of f and g have the same power spectra as those of $\nabla^2 f$ and $\nabla^2 g$, respectively. The respective power spectra for $\nabla^2 f$ and $\nabla^2 g$ are $k^4 |f_k|^2$ and $k^4 |g_k|^2$, where f_k and g_k are the Fourier components of f and g . Each power spectrum equals the corresponding power spectrum of the polarization tensor:

$$\langle |Q_k^{E,B}|^2 \rangle + \langle |U_k^{E,B}|^2 \rangle = k^4 |h_k|^2, \quad (8)$$

where $Q_k^{E,B}$ and $U_k^{E,B}$ are the E and B contributions to the Fourier components of $Q(\equiv (\partial^2/\partial x^2 - \partial^2/\partial y^2)f - 2(\partial^2/\partial x\partial y)g)$ and $U(\equiv (\partial^2/\partial x^2 - \partial^2/\partial y^2)g + 2(\partial^2/\partial x\partial y)f)$, respectively, and h can be either f or g . Equation (8) is very useful since the measured quantity $Y_{E,B}$ can be related to the E and B mode amplitudes directly. In fact, $\nabla^2 f$ and $\nabla^2 g$ are the topological charge and pseudo-charge in the polarization tensor field \mathbf{P} (Chiueh 2000).

Moreover, $Y_{E,B}(R; \mathbf{x}_0)$ is a random variable since the circle may be centered at any arbitrary origins \mathbf{x}_0 . The variance of $Y_{E,B}$ can thus be expressed as:

$$(2\pi R^2)\Delta T_{E,B}(R) \equiv \langle Y_{E,B}^2(R; \mathbf{x}_0) \rangle_{\mathbf{x}_0}^{1/2} = \left[\int_0^\infty |\bar{W}_k|^2 \frac{k^4 |h_k|^2}{2\pi A} k dk \right]^{1/2}, \quad (9)$$

where \bar{W}_k is the Fourier component of \bar{W} , $\langle \dots \rangle_{\mathbf{x}_0}$ stands for the ensemble average of various \mathbf{x}_0 , and A for the area over which the \mathbf{x}_0 surface average is conducted. Here, $\Delta T_{E,B}$ denotes the measured variance of the polarization brightness temperature for mode (E, B) , and the factor $2\pi R^2$ in Eq.(9) arises from the product of two factors: a factor R , which has been multiplied to the data to construct Y in Eq.(2), and the circumference $2\pi R$ of the sky circle for the contour integration. The two factors need to be divided away to obtain the sky surface brightness $\Delta T_{E,B}$. The measured $\Delta T_{E,B}(R)$ contains the polarization spectral information of either mode, subject only to the smearing by a k -space filter $|\bar{W}_k|^2$. The length scale of smearing depends on the radius R , but the details of smearing depend on the power spectrum of the filter function $|\bar{W}_k|^2$.

Finally, we wish to stress that the separation of E and B -modes can, in principle, be achieved with a single-polarization detector. This is because the polarization axis is always rotated to the appropriate direction at every point of the sky circle. One may, for example, align the polarimeter axis to the local radial direction to pick up E_r and integrate E_r^2 over a rotation, and then rotate the axis by 90° to integrate E_ϕ^2 over another rotation. The E mode signal is simply $\langle E_r^2 \rangle - \langle E_\phi^2 \rangle$. For B -mode measurements, one may orient the

polarization axis to either 45° or -45° off the local radial direction, and the B -mode signal is $\langle E_{45^\circ}^2 \rangle - \langle E_{-45^\circ}^2 \rangle$. However, detection of the much weaker B modes with single-polarization detectors may, in practice, suffer from inaccurate calibration of the two measurements to be subtracted from each other.

4. The E -Mode Measurement

Since \bar{W} consists of a top-hat disk and a thin shell, its power spectrum oscillates in the k space at a particular phase with a well-defined frequency comparable to $2R$, the Gibb's phenomenon, and the oscillation amplitude declines as k^{-1} . At the first glance, it appears that such a k -space filter is too extended to be useful. However, this disadvantage may be turned into an advantage for the polarization measurement. The power spectrum of E mode also oscillates in the k space with well-defined frequency and phase. This allows for the possibility that one may adjust the scan radius R to control the oscillation frequency in the power spectrum of \bar{W} so as to optimize the detection of E -mode signals. One would like to match the frequencies of the two oscillations to maximize the overlap of $|\bar{W}_k|^2$ and $|h_k|^2$ in Eq.(9). However, this does not necessarily produce the maximal power since the two oscillations may be out of phase, giving destructive interference. The phase of the k -space oscillation in the E -mode power spectrum is such that it always oscillates asymptotically as $\sin(2\pi k/S)$ for $k/S \geq 2$, where S is the oscillation period; this behavior is rather insensitive to the cosmological parameters, such as Ω_m and Ω_Λ . Most power of $k^2(|Q_k|^2 + |U_k|^2)$ in the E -mode is contained in between $k/S = 2$ and $k/S = 5$. It will turn out that $|\bar{W}_k|^2$ has an optimal phase such that it also oscillates as $\sin(2kR)$. By adjusting the scan radius R so that $R \approx 2\pi/S$, we can obtain an optimal overlap of $|\bar{W}_k|^2$ and $|h_k|^2$, whereby considerable power of the E polarization is captured.

We now turn to show that $|\bar{W}_k|^2 \sim \sin(2kR)/k$ at a large kR . The two dimensional

Fourier transformation of \bar{W} is

$$\begin{aligned}
 \bar{W}_k &= \int [2\Theta(R-r) - r\delta(r-R)] e^{ikr \cos(\phi-\phi_k)} d^2\mathbf{r} \\
 &= \int_0^\infty r dr [2\Theta(R-r) - r\delta(r-R)] \int_0^{2\pi} d\phi \sum_n J_n(kr) e^{in(\pi/2+\phi_k-\phi)} \\
 &= 2\pi \int_0^\infty r dr J_0(kr) [2\Theta(R-r) - r\delta(r-R)] \\
 &= 2\pi R^2 [2\frac{J_1(kR)}{kR} - J_0(kR)] = 2\pi R^2 J_2(kR),
 \end{aligned} \tag{10}$$

where the first term of the third equality arises from the disk and the second term from the shell. The two can be combined to become $2\pi R^2 J_2(kR)$. For $kR \geq 2\pi$, $J_2(kR)$ oscillates as $-\cos(\pi/4 - kR)/\sqrt{kR}$. Thus, $|\bar{W}_k(kR)|^2$ asymptotically oscillates at a frequency $2R$ as $\text{const.} + \sin(2kR)/k$.

To illustrate how the filter function \bar{W}_k captures the oscillating E mode power spectrum, we show $|\bar{W}_k|^2$ for three suitably chosen R 's in Fig.(1a), (1b) and (1c), and compare them with the E -mode power spectra of the Λ CDM model with $\Omega_\Lambda = 0.7$, $\Omega_c = 0.28$ and $\Omega_b = 0.02$, the standard flat CDM model with $\Omega_b = 0.02$, and the open CDM model with $\Omega_c = 0.28$ and $\Omega_b = 0.02$ respectively. Instead of using k , we have used the conventional spherical-harmonics mode number l as the horizontal axis. Identify \mathbf{r} to be the angle on a flat sky, and the relation $l \approx k$ for a large l follows. Moreover, the conventional power spectrum in the spherical harmonic space $C_{E,l}/2\pi$ is replaced by $k^4|f_k|^2/2\pi A$ in Eq.(9). Also shown in Fig.(1) is another $|\bar{W}_k|^2$ for a different choice of R , where the first lobe of $J_2^2(kR)$ is just large enough to enclose the major peaks in the E -mode power spectrum. Such an annulus radius is about a factor of $3 - 4$ smaller than the choice of R that matches the E -mode oscillation. These are the two specific R 's that are expected to capture a substantial power of the E mode.

Plotted in Fig.(2) are the expected $\langle \Delta T_E^2 \rangle$ as functions of the circle radius R in Fig.(2) for the Λ CDM, standard flat-CDM and open-CDM cosmologies, where R is expressed in

unit of arcminute. The primary peak of the polarization brightness corresponds to the smaller one of the two specific R 's shown in Fig.(1a,b,c). It is expected because the first lobe of J_2^2 captures a great deal of the E -mode power. This optimal R 's that yield the peaks in Fig.(2) capture about 10% of the total E -mode power for all three cosmologies.

There exist secondary peaks in Fig.(2), which partially blend into the primary peaks. These secondary peaks are given by the larger R that produces the oscillating $|W_k|^2$ to match the oscillating pattern in the E -mode power spectrum. Apart from the contributions from the two peaks, the E -mode surface brightness is seen to drop rapidly toward large and small R . The Λ CDM and standard flat-CDM cosmologies can hardly be distinguishable at the primary peak except for their different amplitudes. However, the two cosmologies are distinguishable by the secondary peaks. By contrast, the two peaks in the open-CDM cosmology are rather distinct from those of the other two cosmologies in both scale and amplitude.

It is also noted that for $R \geq 100$ arcmin, the E mode power declines by almost a factor of 10 from its respective peak values in the three cosmologies. This is the scale on which one expects to detect the B mode. The E mode on this scale is still much larger than the B mode and may create serious contamination for the B -mode measurement, an issue to be detailed next. In Sec.(7), we will show that a finite beam can cure this problem.

5. *B*-Mode Measurements

Although we have shown the plausibility of the circle projection method for E -mode measurements, a naive application of this method to B -mode measurements may find it difficult to realize, due primarily to the expected ten-times-smaller amplitude in the B mode. As measurements of B modes offer a much greater science return than measurements of E

modes, intense efforts on the B -mode detection are expected to be made in a foreseeable future. The main challenge here is to defeat not only the noise but also the leakage from the much stronger E modes into B modes. According to Eq.(7), the small real part of Y (the B mode) is actually the residue of cancellation among the much stronger E -mode signals along the circle. Therefore, the experimental setup for B -mode measurements can be very different from that for the E -mode. For example, a telescope that is capable of measuring the B mode in a reasonable time span should have a large number of detectors to speed up the observation. In addition, the strategy using single-polarization detectors to measure B mode will likely fail, due to the much weaker signals in the presence of stronger E modes. Hence, dual-polarization detectors are needed for constructing the Stokes Q and U simultaneously.

We shall first briefly review the characteristics of E and B modes. The E -mode power per log-waveband (i.e., $\log k$) peaks at the angular scale about $15 -- 20$ arc-minutes for the currently most favorable Λ CDM cosmology, c.f., Fig.(1a). On the other hand, the B -mode power per log-waveband is less than 1% of that for the E -mode and peaks on the angular scale of a couple of degrees. Adopting the circular projection integration, we show in Fig.(3 a, b, c) how the best choice of $|W_k(R)|^2$ may capture the B -mode power spectra for the three cosmologies indicated in Fig.(1). Plotted in Fig.(4) are the squared variances $\Delta T_B^2(R)$ given by Eq.(9). Note that the peak power captures about 10% of the total B -mode power for all three cosmologies. It is fortunate that the B -mode power concentrates at a much larger scale than where the E -mode power does by almost one order of magnitude. The scale separation can help extract the weak B mode from the CMB polarization in the presence of the strong E mode by adopting an appropriate beam size. This is an important subject to be discussed in Sec.(8).

The N dual-polarization detectors can be regarded as N independent telescopes,

which observe the same sky circle so as to enhance the signal collection power. When each detector rotates around the sky circle at a constant rate, the angular integration becomes time integration. Moreover, each detector does its own time integration without referring to others, and therefore the laborious gain calibration across N detectors is not needed frequently. The leakage from E -modes to B -modes within each detector can in principle be significantly removed after many periods of rotation, a subject to be discussed shortly. The total signal is obtained by summing up the signals collected by each detector after many rotations.

The aforementioned scale separation of E and B modes yields E -mode variations at discrete frequencies $n\Omega$, which is about several to ten times higher than the discrete frequencies of B modes, where Ω is the rotational frequency and n an integer. The present projection method is nothing more than to extract the dc component of the signals. In principle, all E and B modes are periodic in time, and hence the ac signals can be exactly removed in one rotation. In practice, there can be errors introduced in this observing strategy, i.e., the errors in sweeping an exact sky circle at an exact constant rate Ω . These are time-dependent drifts associated with mechanical controls and tend to be of low frequency. They introduce a phase error, i.e., multiplying $c \exp(i\sigma_\omega \alpha(\phi))$ to the integrand of Eq.(7), where c is the efficiency in picking up the E -mode, σ_ω characterizes the error magnitude and $\alpha(\phi)$ is some slow function of ϕ , which is not necessarily periodic in ϕ . If such an error is a random error instead of a systematic error, it is equivalent to broadening the discrete line frequency, $n\Omega \rightarrow n\Omega + \Delta\omega$ with a small random $\Delta\omega$ of variance σ_ω . That is, one should expect that in reality the measured polarization fluctuations are no longer periodic in time, and therefore it may yield some level of E -mode leakage into the B mode. In the worst case, the efficiency of coupling to E modes $c = 1$, and we shall take this limit for the estimation of the leakage below.

The ac E -mode leakage, $\exp[i(n\Omega + \Delta\omega)t]$ of finite n , acquires a complex gain factor

$$G \approx \frac{\sum_{j=0}^N e^{i\Delta\omega(t_j)T}}{n\Omega} \quad (11)$$

after an integration time $T = 2L\pi/\Omega$, where the integer L is chosen to satisfy $L \sim \Omega/2\sigma_\omega$. But the dc B -mode signal gains by a factor NT during the same time interval. The numerator of Eq.(11) can be regarded as random walks with a unit step size and N represents the number of steps. Hence $|G|$ increases with the integration time as $N^{1/2}/n\Omega$, and the signal-to-leakage ratio increases with time as $N^{1/2}n\pi\Omega/\sigma_\omega$.

This estimate is only correct for a finite n . The leakage contributed by the E mode of $n = 0$, which is nearly static and modulated by the low-frequency noise, requires a separate estimate. As mentioned in the last paragraph of Sec.(4), the E -mode power, over a circle of a couple of degrees, is reduced by almost a factor of 10 from its peak value to a level $\sim 8 \times 10^{-13} K^2$ for the Λ CDM cosmology. Note also that the gain factor G is complex, and it is only the imaginary part that can make the dc E mode leak into the dc B mode. Thus, the leakage power from the dc E mode is $\sim 8 \times 10^{-13} K \times (ImG)^2$ after an integration time NT , where

$$ImG \sim T \sum_{j=0}^N \sin(\Delta\omega(t_j)T). \quad (12)$$

It follows that $|ImG| \sim TN^{1/2}$ and the signal-to-leakage ratio increases with time as $N^{1/2}$, which is a factor of $\sigma_\omega/n\pi\Omega (\ll 1)$ smaller than the leakage caused by the ac E modes.

In other words, the dc E mode is the dominant contributor to the leakage. From this estimate, we notice that the extreme low-frequency sweeping errors, such as $1/f$ noise, may seriously hamper the B - E separation. In the estimate below, it is found that N needs to be of order a few hundreds to suppress the E -mode leakage at a satisfactory level. Nonetheless, such extreme low-frequency noise can be efficiently removed when the calibration of the scanning trajectory is conducted periodically. That is, periodic calibration can modulate the low-frequency noise with a finite-frequency, thereby making such noise under control.

To be specific for estimating the number of rotations required to suppress the E -mode leakage, we take the Λ CDM cosmology as a fiducial model. The peak B -mode power is $3.6 \times 10^{-14} K^2$ at the circle radius $R \sim 2$ degrees (c.f., Fig.(4)). On the other hand, the expected E leakage power at this ring radius is $8 \times 10^{-13} N^{-1} K^2$ (c.f., Fig.(2)). Hence, the minimum N is about 70 in order to suppress the leakage down to the 30% level of the expected signal power, and the total number of rotations is therefore $70 \times (\Omega/2\sigma_\omega)$. As mentioned earlier, the lower bound of σ_ω/Ω can be set by periodical calibration. Take $\sigma_\omega/\Omega \sim 0.1$ as an example; one needs 350 rotations to beat down the E -mode leakage satisfactorily. For a total integration time several thousand hours (discussed in Sec.(8)), it requires a rotation rate at least one turn per day. In fact, the leakage from the dc E -mode can be further reduced by the finite beam size. This is the most effective means for E -mode suppression and will be elaborated in Sec.(8) after the effects of finite beam width are examined in Sec.(7).

We now turn to brief discussions on the potentially most serious contaminants to the B -mode measurement. The contamination of the scattered polarized photons from the terrestrial environments, such as the 3-degree CMB photons reflected by the ground and observational instruments, can be a serious problem for the polarization measurement. This problem is even more acute for the B -mode measurement. Nevertheless, uniform illumination of polarized photons to the detector can contribute no net polarization signal after a perfect line integration as the first equality of Eq.(7) shows; neither can the dipole pattern of illuminating sources. In fact, among all multipole patterns, only the quadrupole patterns can contribute to the polarization measurement for the present observing strategy. Serious measures must be taken to guard against the quadrupole-moment scattered lights in the experiment.

The confusion from polarized point sources can also be a serious concern for the CMB

polarization measurement, and they generally contribute almost equally to both E and B modes. They are often synchrotron and dust emission sources; the former is strong at low radio frequencies and the latter dominates at high frequencies(Lin et al. 2002). Since the present method measures small patches of sky in the real space, it is possible to identify the point-source suspects through measurements at very low and very high frequencies *a priori* and to avoid these regions. Point-source confusion may thus be a soluble problem.

6. Temperature Anisotropy-Polarization E-Mode Correlation

The E -mode polarization in the CMBR results from the Thomson scattering off the temperature anisotropy of the primordial adiabatic and/or iso-curvature fluctuations. Therefore, the polarization E -mode is causally related to the temperature anisotropy, with its phase locked to temperature fluctuations. The correlation between the temperature anisotropy scalar field and the polarization tensor field is conventionally defined in the Fourier space as $C_{TE,k} = -k^2 \langle \text{Re}[k^2 f_k T_k^*] \rangle$ per $\log(k)$ band, where $\langle \dots \rangle$ denotes the angular average over the direction of the wave-vector \mathbf{k} . Plotted in Fig.(5,a,b,c) are $C_{TE,k}$ of the same three cosmologies as those indicated in Fig.(1). The averaged signals are a factor of few stronger than those of the E polarization. In the real space, the inverse Fourier transformation gives

$$C_{TE}(r) = \int \frac{d^2 \mathbf{x}_0}{A} \nabla^2 f(\mathbf{r} + \mathbf{x}_0) \Delta T(\mathbf{x}_0). \quad (13)$$

The measured Stokes parameters and temperature anisotropy are subject to different filter functions. While the filter function for the polarization tensor field is \bar{W} , the filter function W_s for the ΔT scalar field is $W_s(r; R) = r\delta(r - R)$. The Fourier component of $W_s(r; R)$ is $W_{s,k}(R) = 2\pi R^2 J_0(kR)$. We define the $T - E$ correlation by multiplying Y_E on the sky circle to the temperature anisotropy on the same circle. The filter-weighted $T - E$

correlation, in unit of temperature, is thus

$$\begin{aligned}\bar{C}_{TE}(R) &= (2\pi R^2)^{-2} \langle Y_E(R; \mathbf{x}_0) \int W_s(r; R) \Delta T(\mathbf{x}_0 + \mathbf{r}) d^2 \mathbf{r} \rangle_{\mathbf{x}_0} \\ &= - \int_0^\infty k^2 \frac{Re[f_k T_k^*]}{2\pi A} J_0(kR) J_2(kR) k dk.\end{aligned}\quad (14)$$

Plotted in Fig.(5 a, b, c) are also the composite filter function $J_0(kR)J_2(kR)$ of some choices of R for the three cosmologies. Figure (6) shows $\bar{C}_{TE}(R)$ as functions of R in unit of arcminute. As $C_{TE}(R)$ is not a positive definite quantity, the spatial filtering significantly smears out the $T - E$ correlation and the resulting \bar{C}_{TE} gives a relatively small signal strength for all filter sizes R . Thus, applying the circular-contour integration to measure $T - E$ correlation is probably not an optimal strategy. Nevertheless, if an experiment has a sufficiently high sensitivity to detect the E -mode variance, it should also be well within its capability to measure \bar{C}_{TE} .

7. Effects of Finite Beam Width

In a real experiment, the detector beam has a finite width. Even with a finite beam width, the present strategy for separating E and B modes still holds. Below, we specifically consider the scanning-beam observation with a single detector, where the polarimeter axes are rotated to align with the local radial and azimuthal directions defined by the beam-center position \mathbf{R} . Moreover, the beam also co-rotates with the polarimeter axes so that its orientation remains fixed with respect to the local radial direction. Such a setup measures the following surface brightness weighed by the beam around the circle:

$$\begin{aligned}Sb(\mathbf{r}) &= -i \int_0^{2\pi} \frac{d\phi_R}{2\pi} A(\mathbf{r} - \mathbf{R}) [(\cos(2\phi_R)Q + \sin(2\phi_R)U) + i(\cos(2\phi_R)U - \sin(2\phi_R)Q)] \\ &= -i \int_0^{2\pi} \frac{d\phi_q}{2\pi} e^{i2(\phi_R - \phi)} A(\mathbf{r} - \mathbf{R}) \\ &\quad [r \frac{\partial}{\partial r} (\frac{1}{r} \frac{\partial}{\partial r}) - \frac{1}{r^2} \frac{\partial^2}{\partial \phi^2} + \frac{2i}{r} \frac{\partial}{\partial \phi} (\frac{\partial}{\partial r} - \frac{1}{2r})] (f + ig),\end{aligned}\quad (15)$$

where the second equality of Eq.(7) has been used, $A(\mathbf{r} - \mathbf{R})$ is the rotating beam pattern, and ϕ_R the azimuthal angle of the beam center. The beam-center angle ϕ_R , instead of ϕ , appears on the right of the first equality because the rotation of polarimeter axes always refers to the beam-center position on the circle. The beam pattern A can generally be expanded in terms of the monopole, quadrupole, etc.. When the beam pattern co-rotates with the polarimeter axis, both angles ϕ_R and ϕ always appear in these multipole moments in the combination, $\phi - \phi_R$. Hence when the beam-center angle ϕ_R is integrated out, we obtain an additional radial window function to account for the fact that the finite-size beam measures a sky annulus of finite width rather than an infinitely sharp ring, as illustrated below. The radial window function is a real quantity, and therefore the separability of B and E modes remains intact.

For the purpose of illustration, we let the beam be symmetric Gaussian with a half width d , though in practice the beam is not necessary a symmetric one,

$$\begin{aligned}
 A(\mathbf{r} - \mathbf{R}) &= e^{-(\mathbf{r}-\mathbf{R})^2/2d^2} \\
 &= e^{-(r^2+R^2-2rR\cos(\phi-\phi_R))/2d^2} \\
 &= \sum_n I_n(rR/d^2) e^{in(\phi-\phi_R)} e^{-(r^2+R^2)/2d^2}, \tag{16}
 \end{aligned}$$

where the circle has been taken to have a radius R , and I_n is the modified Bessel function. The effective area of the beam is $2\pi d^2$. The angular average of ϕ_R of Eq.(15) can then be carried out without involving ϕ , and it follows that

$$Sb(\mathbf{r}; R, d) = -iI_2(rR/d^2) e^{-(r^2+R^2)/2d^2} [r \frac{\partial}{\partial r} \left(\frac{1}{r} \frac{\partial}{\partial r} \right) - \frac{1}{r^2} \frac{\partial^2}{\partial \phi^2} + \frac{2i}{r} \frac{\partial}{\partial \phi} \left(\frac{\partial}{\partial r} - \frac{1}{2r} \right)] (f + ig). \tag{17}$$

In the case when the beam is asymmetric, this method also works, as long as the beam shape remains fixed with respect to the local rotating coordinate around the circle. For example, when the beam has a quadrupole component, the beam

$A(\Delta\mathbf{r}^2/2d^2)$ ($\equiv A(\mathbf{r} - \mathbf{R})^2/2d^2$) in Eq.(16) will need to be replaced by

$$A\left[\frac{1}{4}(b^{-2} + a^{-2})\Delta\mathbf{r}^2 + \frac{1}{4}(b^{-2} - a^{-2})((\Delta x^2 - \Delta y^2)\cos(2\phi_R) + 2\Delta x\Delta y\sin(2\phi_R))\right], \quad (18)$$

where a and b are the long and short axes, respectively, and the ϕ_R -dependence accounts for the co-rotating beam pattern. The quadrupole moment in the argument of A can be re-arranged to become $(1/4)(b^{-2} - a^{-2})[r^2(\cos(2(\phi - \phi_R)) - 1) + (\Delta\mathbf{r})^2]$. When such a beam is substituted into Eq.(15), the result is similar to Eq.(17) except for a different radial function in Eq.(17). This nice result allows us to carry out the next manipulation for projecting out the E and B modes as shown below. (We shall not dwell on asymmetric beams in the following discussions, but only to point out here that asymmetric beams pose no problem for the proposed $E - B$ separation.)

We now perform an angular average of Eq.(17) over ϕ , corresponding to retaining only the dc component of the signals, and find that

$$\bar{S}b(r; R, d) = -iI_2(rR/d^2)e^{-(r^2+R^2)/2d^2}\left[r\frac{\partial}{\partial r}\left(\frac{1}{r}\frac{\partial}{\partial r}\right)(\langle f \rangle(r) + i\langle g \rangle(r))\right]. \quad (19)$$

The real and imaginary parts correspond to the B and E modes, respectively. Identical to what we have found in Sec.(2), Eq.(19) can be re-written as a surface convolution with a window function \bar{W} :

$$\bar{S}b(r; R, d) = i[I_2(rR/d^2)e^{-(r^2+R^2)/2d^2}]\int \frac{d^2\mathbf{r}'}{2\pi r^2}\bar{W}(r - r')\nabla'^2(f(\mathbf{r}') + ig(\mathbf{r}')) \quad (20)$$

where $\bar{W}(r - r') \equiv 2\Theta(r - r') - r\delta(r' - r)$. The squared bracket in Eq.(20) sharply peaks at $r = R$ when the primary beam width $d \rightarrow 0$; it becomes $\delta(r - R)/2\pi R$ and Eq.(20) is then reduced to Eq.(7) of the sharp-beam case.

Moreover, the convolution surface integral of \mathbf{r}' in Eq.(20) can further be expressed as

$$\int \frac{d^2\mathbf{r}'}{2\pi r^2}\bar{W}(r - r')\nabla'^2h(\mathbf{r}') = \int \frac{d^2\mathbf{k}}{4\pi^2}J_2(kr)k^2h_k, \quad (21)$$

after an identical algebra as before. Finally, the averaged surface brightness over the whole beam becomes

$$\begin{aligned}
 \Delta T(R, d) &= \int d^2 \mathbf{r} \frac{\bar{S}b(r; R, d)}{2\pi d^2} \\
 &= i \int \frac{d^2 \mathbf{k}}{4\pi^2} \left[\int \frac{d^2 \mathbf{r}}{2\pi d^2} J_2(kr) I_2(rR/d^2) e^{-(r^2+R^2)/2d^2} \right] k^2 (f_k + ig_k) \\
 &= i \int \frac{d^2 \mathbf{k}}{4\pi^2} J_2(kR) e^{-(k^2 d^2/2)} k^2 (f_k + ig_k)
 \end{aligned} \tag{22}$$

and its variance

$$\Delta T_{E,B}(R, d) = \left[\int_0^\infty J_2^2(kR) e^{-k^2 d^2} \frac{k^4 |h_k|^2}{2\pi A} k dk \right]^{1/2}, \tag{23}$$

where $|h_k|^2$ represents either $|f_k|^2$ or $|g_k|^2$. When $kd \ll 1$, we recover the sharp-beam limit, Eq.(9), from Eq.(23). Figure (7) plots the squared variance of the beam weighed surface brightness of E and B modes as a function of the annulus radius R with various d 's for the fiducial Λ CDM cosmology ($\Omega_\lambda = 0.7$, $\Omega_{cdm} = 0.28$ and $\Omega_b = 0.02$). The non-zero d leads to smearing of the peaks appearing in the sharp-beam limit. Moreover, the drastic decline in the E -mode power for a non-negligible kd is also evident in Fig.(7). This is due to the Gaussian cutoff in Eq.(23).

Similarly, when observed with a finite beam, the $T - E$ correlation, Eq.(14), becomes

$$\bar{C}_{TE}(R, d) = - \int_0^\infty k^2 \frac{Re[f_k T_k^*]}{2\pi A} J_0(kR) J_2(kR) e^{-k^2 d^2} k dk. \tag{24}$$

Shown in Fig.(8) are the $T - E$ correlation of the fiducial cosmology for various d 's. Apparently, the Gaussian cutoff is also at work when the beam width is non-negligible.

8. Discussions

We return to the discussions on the E -mode leakage to the B -mode measurements, especially when the effects of finite beam width are taken into account. Fig.(7) clearly

shows that when the half-beam width $d \sim 17$ arcmin, the peak B -mode power decreases from the sharp-beam case by a factor about 1.3. But with such a wide beam, the E -mode power decreases by a factor of 10, as compared with the sharp-beam case, at the radius $R \sim 2$ degrees. Hence the E -mode power is only a factor of 3 greater than that of the B -mode power around $R \sim 2$ degrees. This is due precisely to the scale separation between E and B modes; the wide beam yields a small kd for B modes but a sizable kd for E modes. That is, one can always choose an appropriate beam to significantly suppress the E -modes leakage while not to sacrifice the B -modes. For the Λ CDM cosmology, a half-beam of 17 arcminutes is near the optimal for B -mode detection.

We are now in a position to estimate how likely the B and E modes may be detected by the circular scan strategy in the near future. The AMiBA experiment(Lo et al. 2000) is equipped with two separate sets of 19 dishes of different sizes, 30cm and 120cm, mounted on a 6m turntable platform. It has 20-GHz wide-band receivers with dual polarization capability and operates at 90 GHz, a frequency window in which the Galactic synchrotron and dust emissions are both minimal. The AMiBA has been designed to operate in the interferometry mode, which has the advantage of easily removing systematic errors. However, AMiBA can also operate in the single-dish mode, to which the present observing strategy applies. In each single dish, both left and right circular-polarization detectors collect independent signals, and the two sets of signals are correlated to obtain the Stokes Q and U . Much like the conventional interferometric measurements, correlation of the two independent signals can significantly remove the systematic errors as well as the electronic $1/f$ noise. With the system temperature $T_s = 70$ K, bandwidth $\Delta\nu = 20$ Ghz, and antenna efficiency $\eta_a = 70\%$ for AMiBA, the noise level per antenna per polarization after an integration time t_{int} is $1.22 \times (\sqrt{2}T_s / \sqrt{\eta_a^2 t_{int} \Delta\nu})$ and it amounts to $1.2\text{mK}/\sqrt{t_{sec}}$, where the factor 1.22 corrects for the non-Rayleigh-Jeans limit for 90 Ghz and t_{sec} is t_{int} in unit of seconds. With 19 antennae and dual polarization, the system noise is reduced by $\sqrt{38}$ to

become $200\mu\text{K}/\sqrt{t_{sec}}$.

Thus, in 3.8-hour integration, one obtains a noise level down to $1.7\mu\text{K}$, which is the expected maximum surface brightness of the E mode with the 1.2m AMiBA dish, or $d = 4.2'$ in Fig.(7). In 35 hours, a 3σ E -mode signal is expected in a single sky annulus of radius in between 15 and 30 arcminutes. The B -mode peak strength for the AMiBA 0.3m dish, ($d = 17'$ in Fig.(7)) is about $0.18\mu\text{K}$. It therefore requires about 340 hours to detect an 1σ signal, or 3000 hours for a 3σ B -mode signal in a single annulus of radius 2 degrees or so.

So far, we have estimated the signals for the single-field measurement, which are in themselves random fluctuations. To beat down the sample variance and construct the B -mode curves shown in Fig.(7), one needs a more efficient approach for determining the variance of the random signals in the presence of the instrument noise than the deep measurement described above. The combined error $\delta(\Delta T^2)$ of the sample variance and instrument noise is estimated to be

$$\frac{\delta(\Delta T^2)}{\Delta T^2} = \frac{\sqrt{2}(1 + \sigma_n^2/\Delta T^2)}{\sqrt{N_{sam}}}, \quad (25)$$

where σ_n is the variance of the instrument noise per sky annulus and N_{sam} the number of independent sky annuli measured. Note that $\sigma_n^2 \propto t_{int}$, $\Delta T^2 \propto t_{int}^2$ and the total observing time is $N_{sam}t_{int}$. For a fixed total observing time, we want the single-field integration time t_{int} such that $(\sigma_n/\Delta T)^2 \sim 1$. That is, the optimal strategy for the determination of the curves shown in Fig.(7) is to collect signals with $S/N = 1$ per sky annulus. Thus, the desired integration time per annulus for the B mode is therefore $t_{int} = 340$ hours for AMiBA with a 17 arcmin half-beam. The determination of $\langle \Delta T_B^2 \rangle$ at the 3σ level (including the sample variance) requires $N_{sam} = 72$ or a total integration time 2.5×10^4 hours. This amount of total observing time has become too long to be realistic.

Having discussed the capability of AMiBA for the CMB polarization measurement,

we briefly turn to a discussion on the optimal instrument that may be able to realistically measure a substantial part of the B -mode curve shown in Fig.(7). The guiding principle for an optimal telescope is to collect as many photons as possible, and it thus requires as large a light collecting area as possible for a fixed beam size. However, the conventional radio telescopes mostly work in the diffraction-beam regime, where $A_{phy}\Omega_b/\lambda^2 \sim 1$ with A_{phy} , Ω_b and λ being the physical area of the telescope, the beam solid angle and the photon wavelength, respectively, for the reason that these telescopes are designed to maximize the angular resolution for conventional observations. However, the B modes are intrinsically of large scale (degree scale), and the measurements of B modes thus require low-resolution telescopes. From the discussions given in the beginning of this section, we see that a half-beam width about 17 arcmin can just be appropriate for the B -mode measurement. At $\nu = 90\text{GHz}$, the dish diameter of a conventional radio telescope that yields a diffraction beam of 17 arcmin is about 0.3 meters. Such a conventional telescope is not optimized. An optimized telescope should adopt multi-mode feeds, where the antenna beam may be made much wider than the diffraction beam. That is, for a fixed beam width, one would like to increase the dish size as much as possible. (Note that the surface brightness signal-to-noise ratio increases linearly with the dish area.) As an example, a 2-meter dish with a 17-arcmin half beam is 45 times more sensitive than a 0.3-meter dish with a 17-arcmin half beam. A large-dish telescope hence has a tremendous advantage over an instrument such as AMiBA, which consists of 19 dishes of 0.3-meter diameter with diffraction beams. With the same noise temperature per detector, such a 2-meter, single-detector telescope gains a factor 10(\propto (ratio of dish area)(ratio of detector number) $^{1/2}$) in detection sensitivity over AMiBA, or a factor 10^2 reduction in the integration time, thereby making the B -mode power spectrum measurement a feasible task to conduct.

However, there is a caveat for this multi-mode feed approach. The beam pattern and the polarization property can be difficult to control. To attain the sensitivity given by the

above example, 45 modes are needed; the multi-mode bolometer currently in operation contains 10 modes or so for the Maxima experiment (private conversation with Paul Richards). Despite the technical challenges, it is certainly worthwhile to contemplate the next generation experiments for B -mode measurements along this direction.

9. Conclusion

In sum, this work addresses how the CMBR polarization E and B modes can be separated with a local measurement of Stokes parameters Q and U . For scanning observations, we show that the only scanning trajectory capable of separating E and B polarization patterns are those that are circles. Moreover, the polarimeter axis also needs to rotate along the circle at the same rate as well. By varying the annulus radius R , one can measure E and B modes of various scales. In terms of the conventional power spectrum, this circular scanning observation is equivalent to adopting some particular k -space filters. We have presented the expected surface-brightness of E and B modes as well as the $T - E$ correlation measured through these filters.

Though such a detection strategy contains only the gross information of the polarization power spectrum, it nevertheless exhibits the following good features:

- (a) The measured peak power of E and B modes can be about 10% of the total power contained in the CMB polarization fluctuations. The relatively high efficiency makes this strategy attractive for the detection of E and B polarization fluctuations in the CMB.
- (b) The measurement can be conducted on a turntable platform, where all detectors scan the same sky circle, with each detector performing its own integration of Stokes Q and U . The noise in the N detectors are all independent and the data gathered by each detector can be straightforwardly summed together to enhance the signal-to-noise ratio.

This sweeping-beam strategy is particularly useful for the weak B -mode detection, as the scan can be on an almost perfect circle, which is needed to avoid the E -mode leakage. The sweeping-beam strategy also avoids the need for frequent calibration across different detectors, thereby making the observation simple and stable.

- (c) The present observing strategy is perfectly valid when the beam has a finite size. This opens up the possibility that one may effectively suppress the E -mode leakage to the measurements of B modes, and the possibility that the observation of the weak CMB polarization signals can be made efficiently by using a large telescope with a finite beam, a beam that is much larger than the diffraction beam.
- (d) Even when the beam is asymmetric the circular scan strategy remains valid, provided that the beam shape and orientation remain fixed with respect to the local axes along the circle traced by the beam center.
- (e) The present method measures, in effect, the combination of a circular-top-hat-filtered and a circular-ring-filtered polarization patterns. In the Fourier domain, both power spectra of the combined filter and the E mode oscillate. There exists a filter (primarily the ring filter) of size R for the two oscillations to have the same frequencies and phases, so that a substantial power of E mode is picked up. It results in a second peak in the E -mode surface brightness, which can be used to distinguish the Λ CDM cosmology from the SCDM cosmology, as shown in Fig.(2).
- (f) The measurement is in real space, and it can be sensitive to the spatially localized non-Gaussian features, which can be either genuine CMB signals or confusion radios sources(Lin et al. 2002).

Thus, with the above advantages, the present local observational strategy offers an alternative way to detect the CMBR polarization for the ground-based or balloon-borne

experiments, where the observation is confined within a relatively small patch of sky. This method is particularly useful for B -mode measurements, since B -mode signals are so weak that deep exposure is indeed needed.

Interestingly, the present method of circular scan can also be applied to the interferometric measurements of CMBR polarization(1), an observational strategy that originally aims to directly extract the Fourier power spectrum rather than making the real-space map. The details of how it can be achieved will be reported in a separate paper.

After the submission of this work, we noted a relevant work appearing in the literature(Lewis et al. 2002), which addresses the extraction of B modes in a circular patch of sky. By suitable linear combinations of signals obtained from different concentric sky annuli, it is possible to extract, apart from the axisymmetric modes, the non-axisymmetric B modes.

We thank the AMiBA team for useful discussions. T.C would also like to thank Jeff Peterson and Paul Richards for discussions on the workings of the multi-mode feed bolometer. This work is supported in part by the National Science Council of Taiwan under the grant NSC90-2112-M-002-026.

REFERENCES

Bond, J.R. & Efstathiou, G. 1984, ApJ, 285, L45

Chiueh, T. 2000, arXiv:astro-ph/0010433

Chiueh, T. & Ma, C.J., 2000, "Proceedings of Texas Symposium on Relativistic Astrophysics", Austin, Texas.

Chiueh, T., Lin, H.C. & Ma, C.J., 2001 (in preparation).

Crittenden R.G., Natarajan P., Pen, U.L. & Theuns, T., 2000, arXiv:astro-ph/0012336

Hu, W. & White M. 1997, Phys. Rev. D56, 596

Kaiser, N., Squires, G., Fahlman, G. & Woods, D. 1994, in "Cluster of Galaxies" eds. F. Durrett, A. Maxure, and J. Tran Thanh Van, Editions Frontieres, Gif-sur Yvette, p.269

Kamionkowski, M., Kowsowsky, A. & Stebbins, A. 1997, Phys. Rev. D55, 7368

Lewis, A., Challinor, A & Turok, N. 2002, Phys. Rev. D65, 23505

Lin, H.C., Chiueh, T. & Wu, X.P. 2002, astro-ph/0202174

Lo, K.Y., Chiueh, T., Liang, H., Ma, C.P., Martin, R., Ng, K.-W., Pen, U.L. & Subramanyan, R. 2000, IAU Symp. no. 201, 31

O'Dell, C., Keating, B. & Timbie, P. 2000, AAS 197, 17080

Polnarev, A.G. 1985, Sov. Astron., 29, 607

Rees, M.J. 1968, ApJ, 153, L1

Revenu, B., Kim, A., Ansari, R., Couchot, F., Delabrouille, J. & Kaplan, J. 2000, A& As. 142, 499

Seljak, U. & Zaldarriaga, M. 1998, in "Fundamental Parameters in Cosmology" proceedings of the XXXIIrd Rencontres de Moriond 1998, arXiv:astro-ph/9805010

Staggs, S.T., Gunderson, J.O. & Church, S.E., 1999, arXiv:astro-ph/9904062

Tegmark, M. & de Oliveria-Costa, A., 2000, arXiv:astro-ph/0012120

White, M., Carlstrom, J. E., Dragovan, M. & Holzapfel, W. L. 1999, ApJ, 514, 12

Zaldarriaga, M. & Seljak, U. 1997, Phys. Rev. D55, 1830

Zaldarriaga, M. 1998, ApJ, 503, 1

Fig. 1.— Fig.(1 a,b,c): The power spectra of E -modes $l(l+1)C_{E,l}/2\pi$ (solid lines) for the (a) Λ CDM with $(\Omega_\Lambda, \Omega_{cdm}) = (0.7, 0.28)$, (b) standard flat-CDM, and (c) open CDM cosmologies. Superposed on the power spectra are the (arbitrarily scaled) k -space filter functions $|\bar{W}_k(R)|^2 (= J_2^2(kR))$ of two particular annulus radii R (dotted and dashed lines), which are optimaized to capture the features in the power spectra.

Fig. 2.— Fig.(2): The squared variances ΔT_E^2 as functions of the annulus radius R for the three cosmologies of Fig.(1). ΔT_E^2 is in unit of K^2 and R in unit of arcminute.

Fig. 3.— Fig.(3 a,b,c): The power spectra of B modes $l(l+1)C_{B,l}/2\pi$ (solid lines) for the three cosmologies (a,b,c) of Fig.(1). Superposed on the power spectra are the (arbitrarily scaled) k -space filter functions $|\bar{W}_k(R)|^2 (= J_2^2(kR))$ of the optimized R 's that capture the power of the B modes (dotted lines).

Fig. 4.— Fig.(4): The squared variances ΔT_B^2 as functions of R for the three cosmologies. The units are the same as in Fig.(2).

Fig. 5.— Fig.(5 a,b,c): The $T - E$ correlation spectra $l(l+1)C_{TE,l}/2\pi$ (solid lines) for the three cosmologies (a,b,c). Superposed on the correlation spectra are the k -space filter functions $J_0(kR)J_2(kR)$ for some choice of R 's. Hardly can any choice of R yield k -space filter functions that oscillate in phase with the correlation spectra.

Fig. 6.— Fig.(6): The filtered $T - E$ correlation \bar{C}_{TE} as functions of R for the three cosmologies. The units are the same as Fig.(2). The signal strengths are seen to be substantially lower than the peaks in Fig.(5).

Fig. 7.— Fig.(7): The finite-beam effects on the detected E and B -mode surface brightness as functions of the radius R of sky annulus and of various half-beam widths d for the fiducial Λ CDM cosmology. The reduction of surface brightness is due to the Gaussian cutoff of finite

beam in the window function as indicated in Eq.(22).

Fig. 8.— Fig.(8): The finite-beam effects on the detected $T - E$ correlation as functions of R and of d for the fiducial Λ CDM cosmology.

Fig. 1a

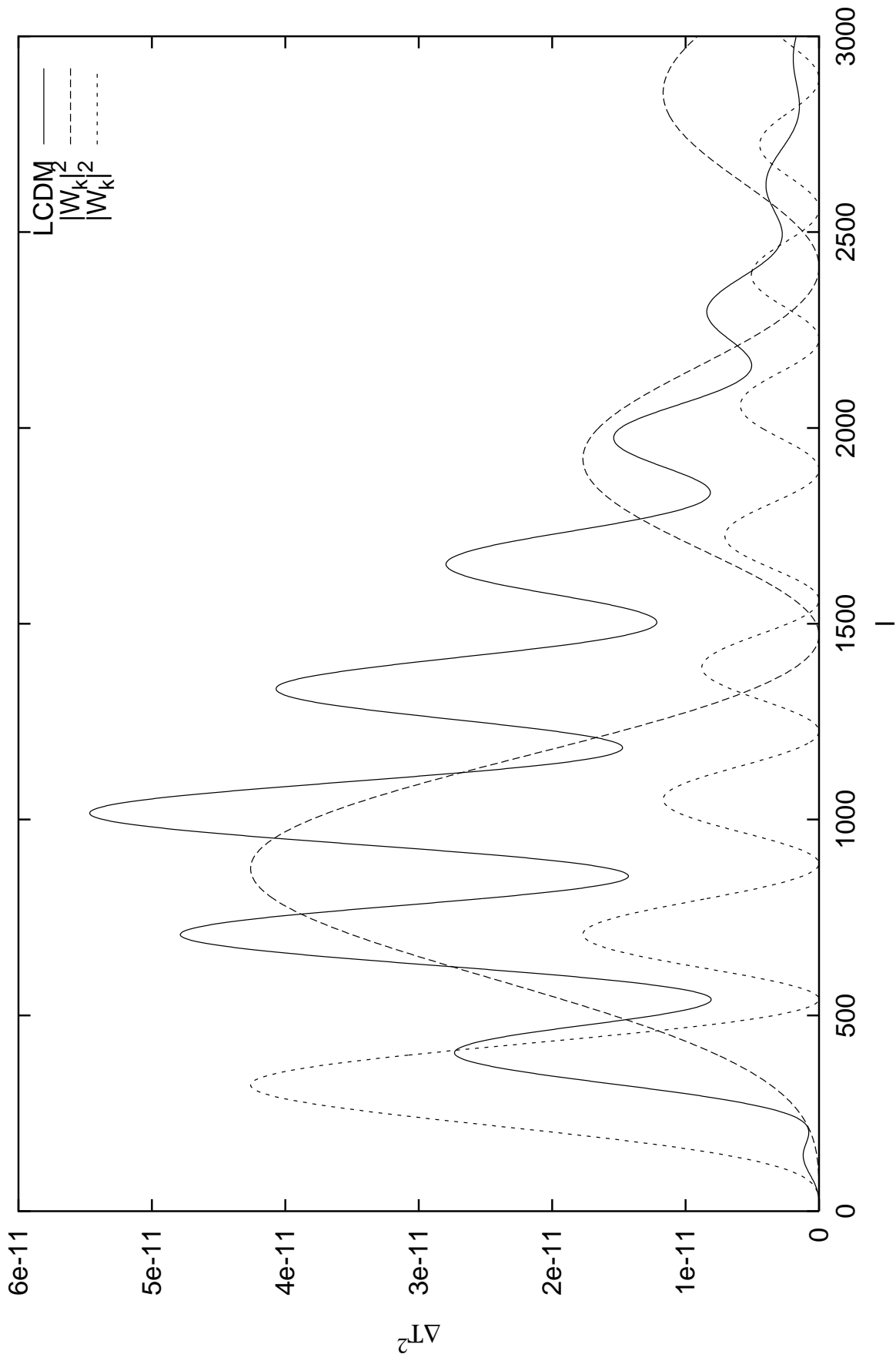


Fig. 1b

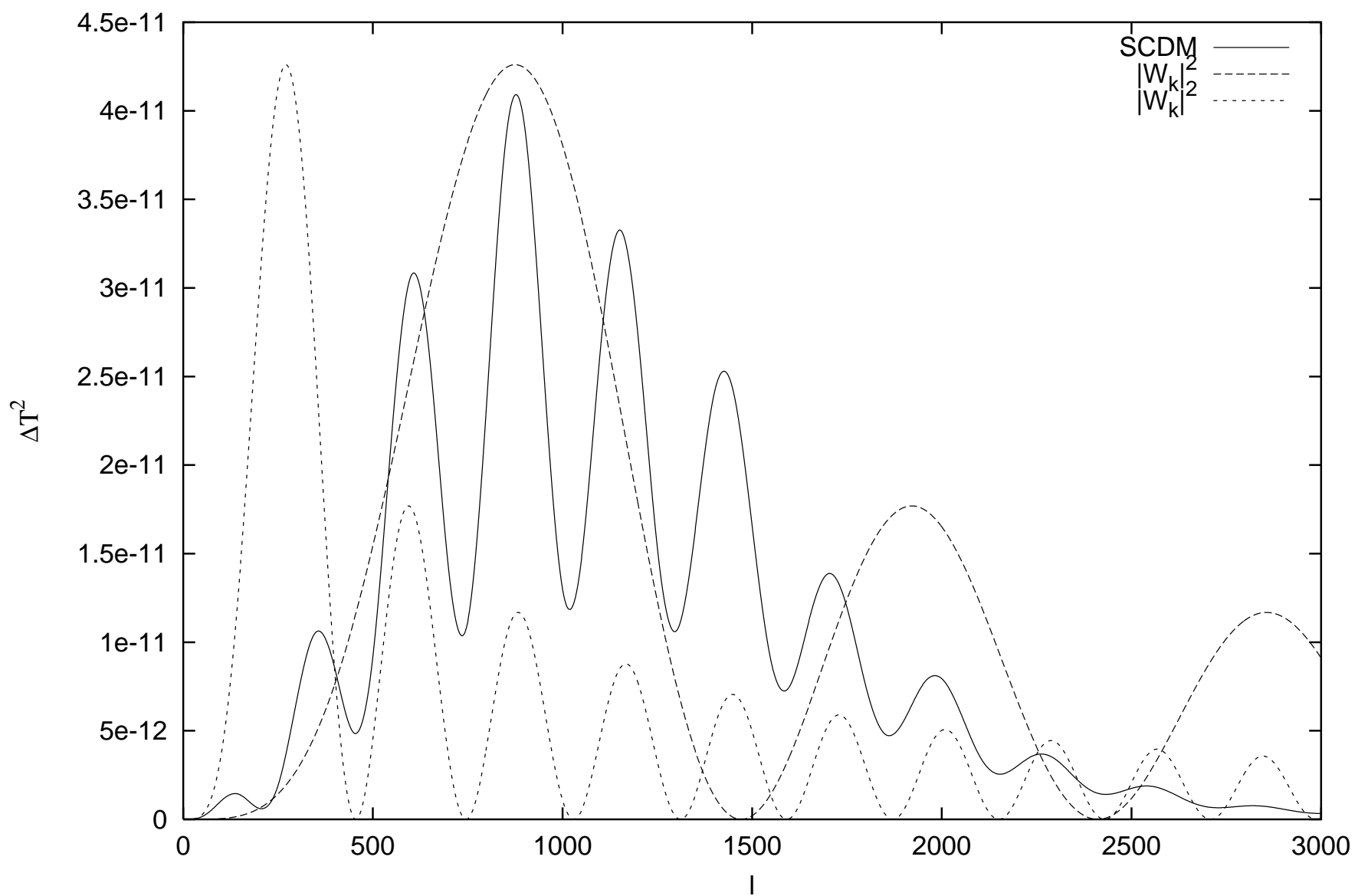


Fig. 1c

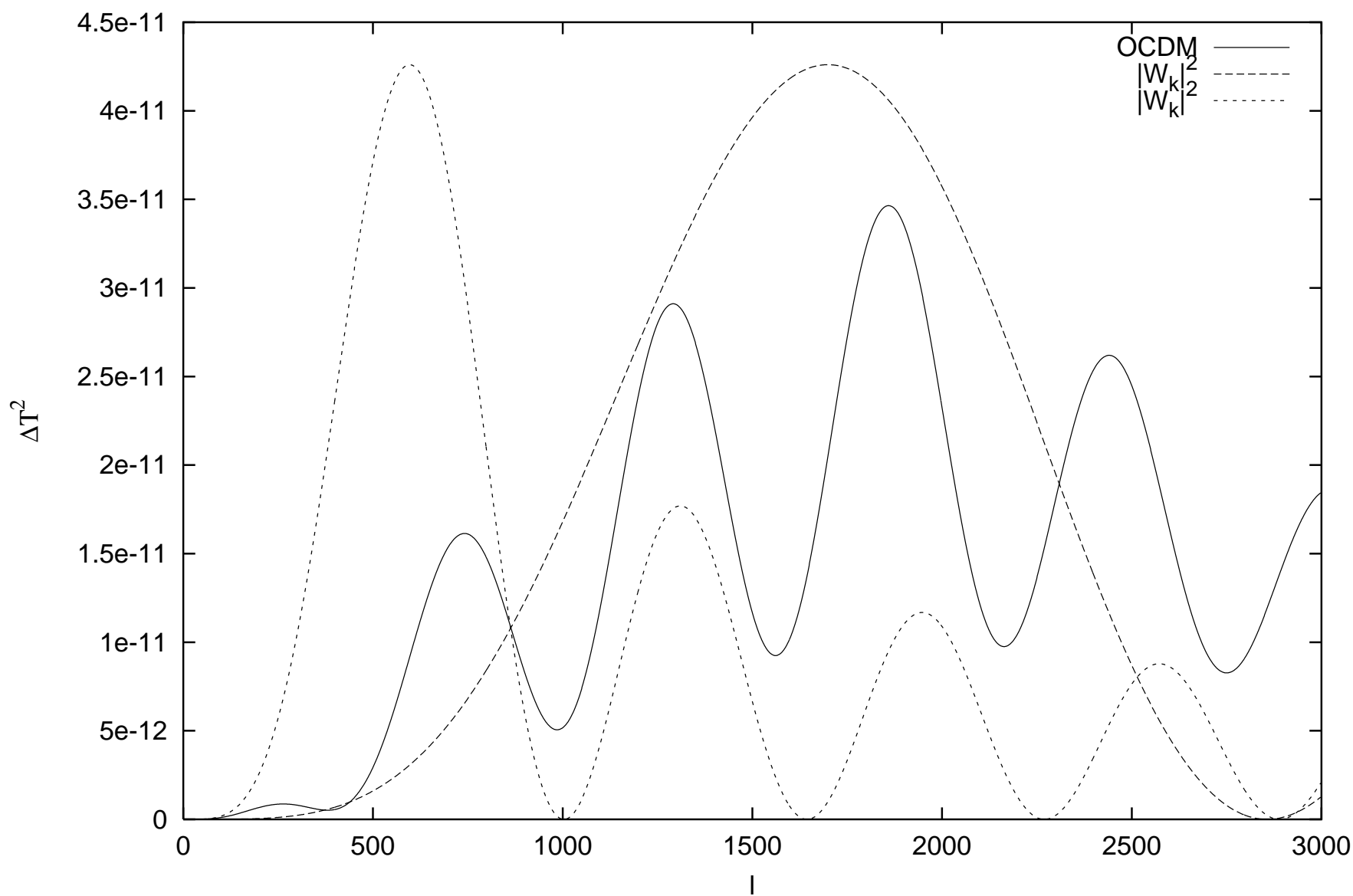


Fig. 2

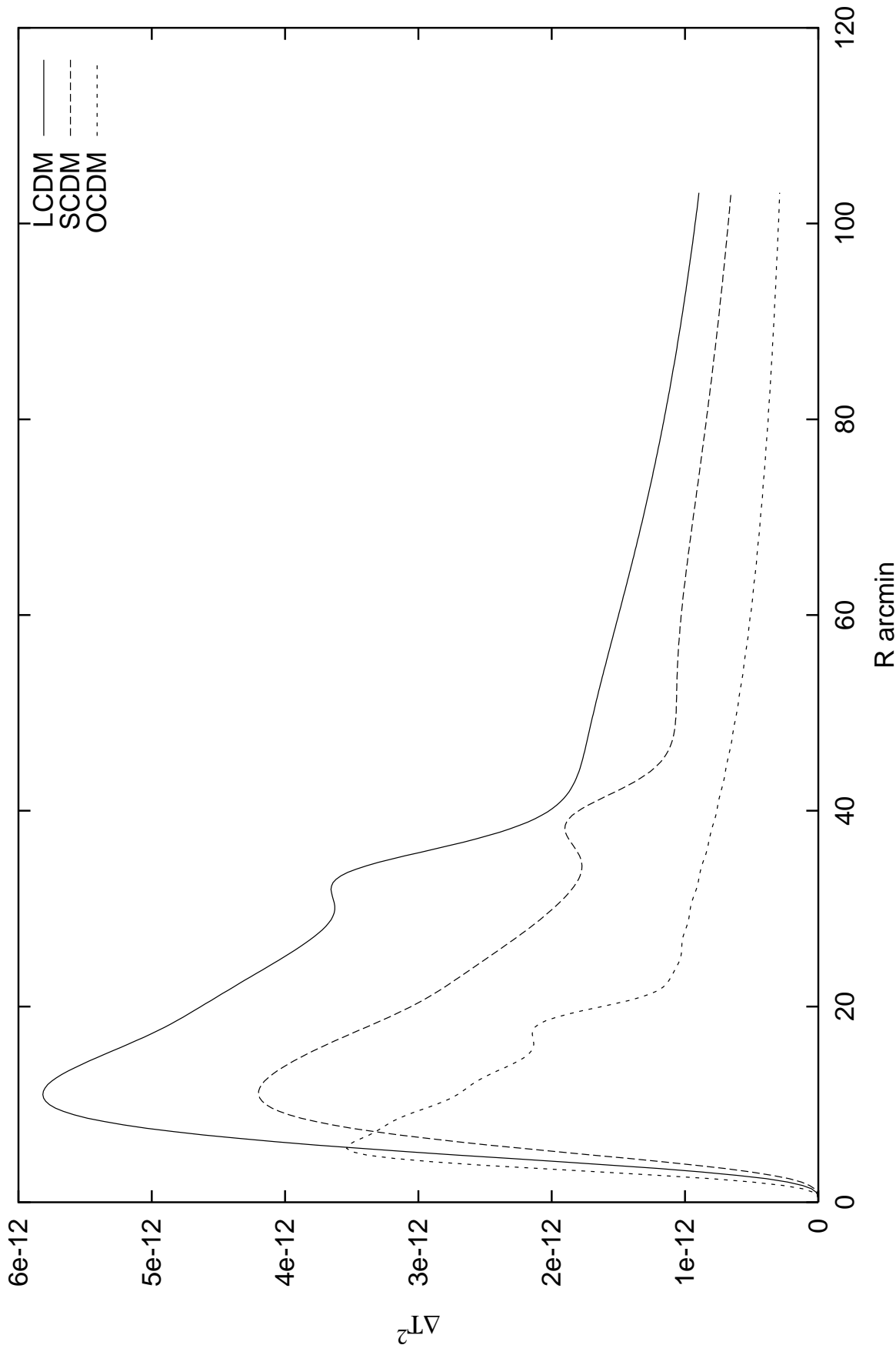


Fig. 3a

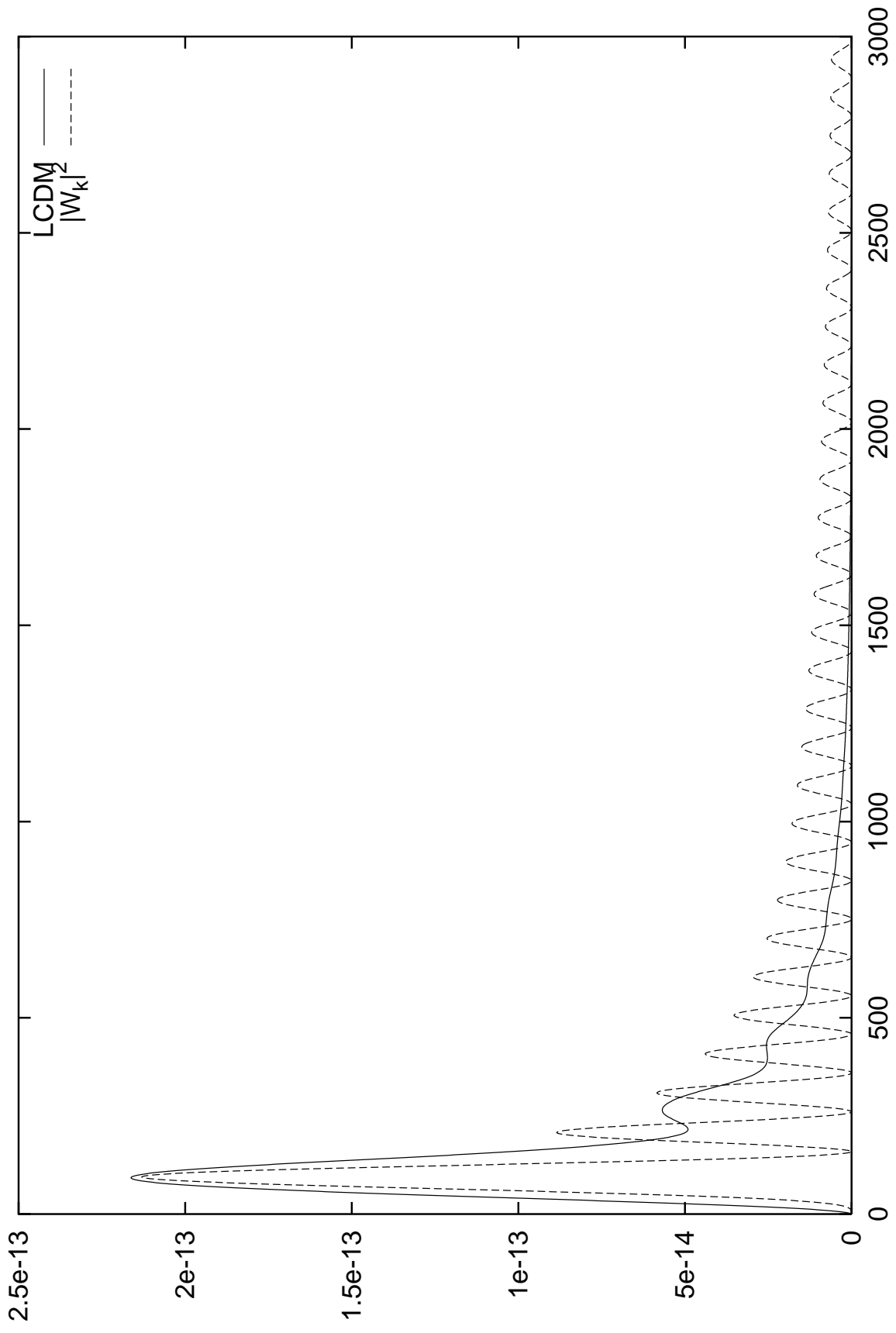


Fig. 3b

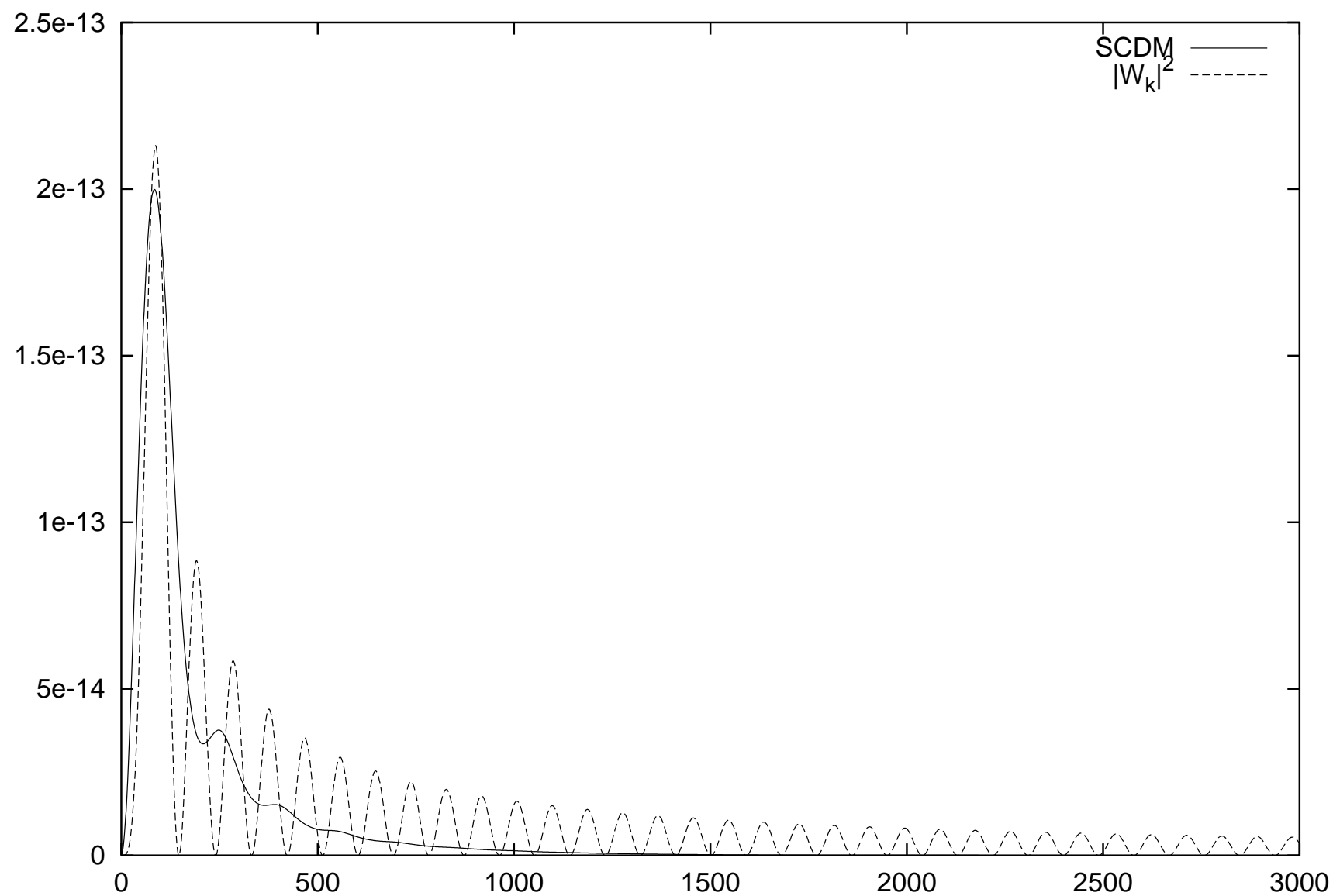


Fig. 3c

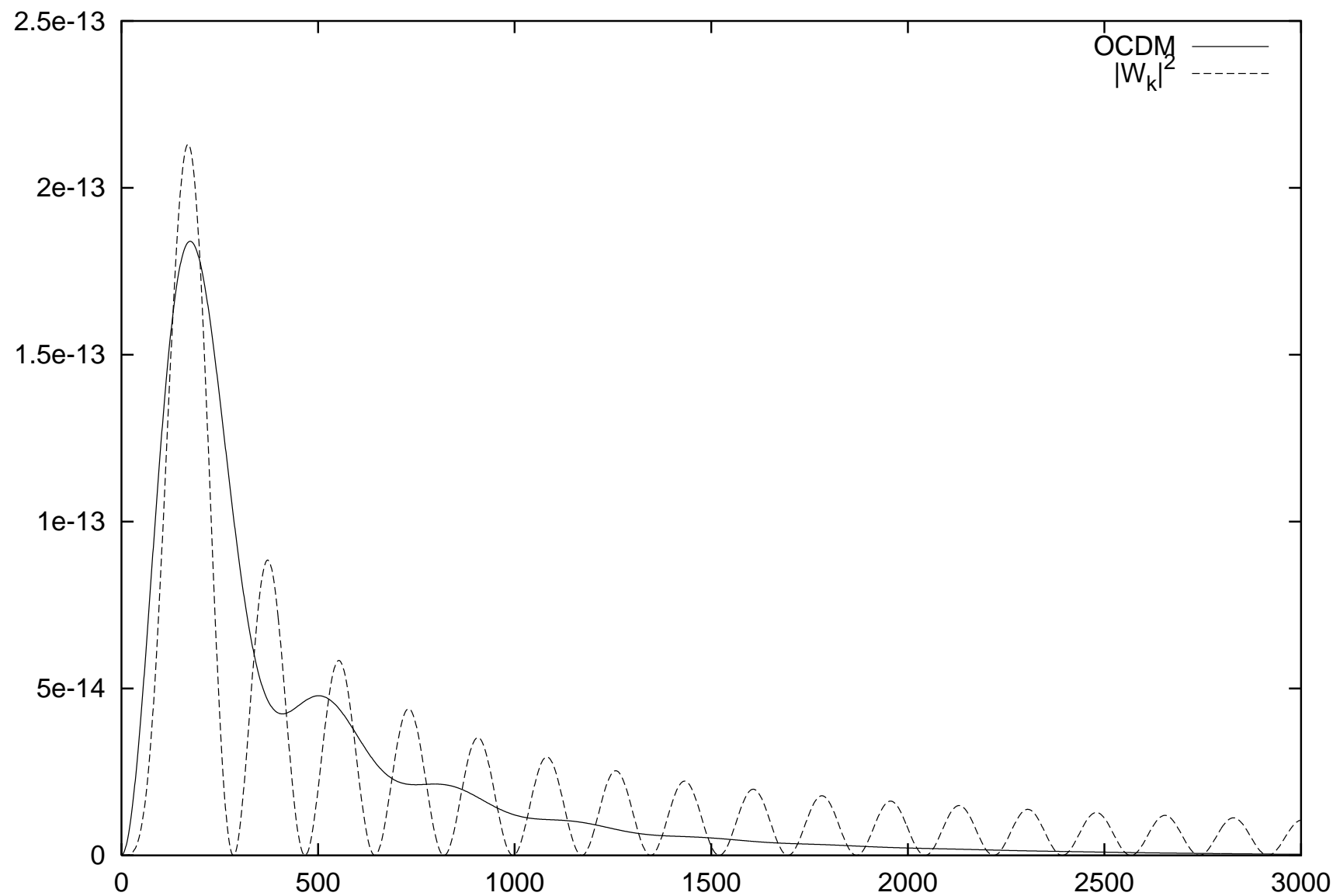


Fig. 4

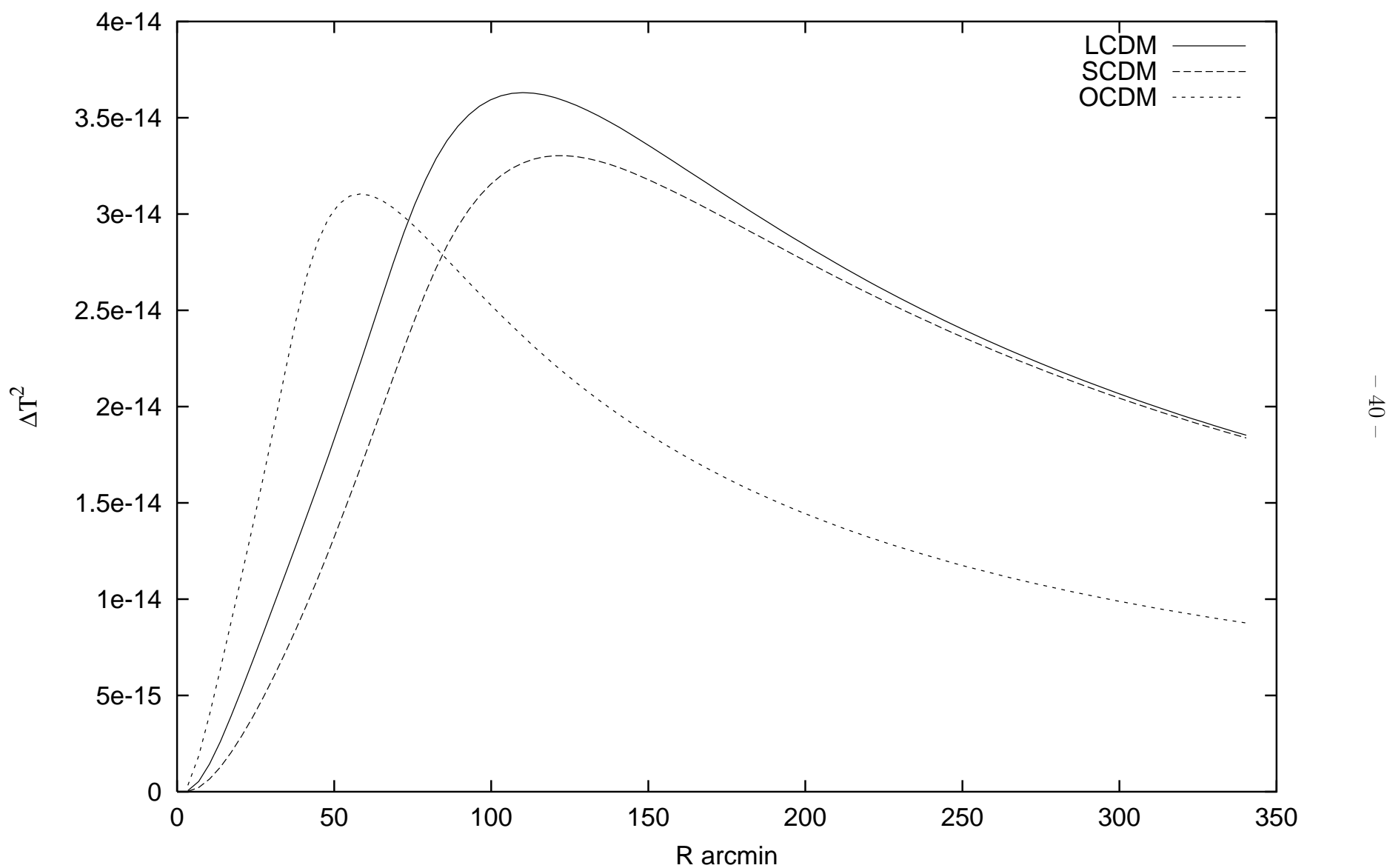


Fig. 5a

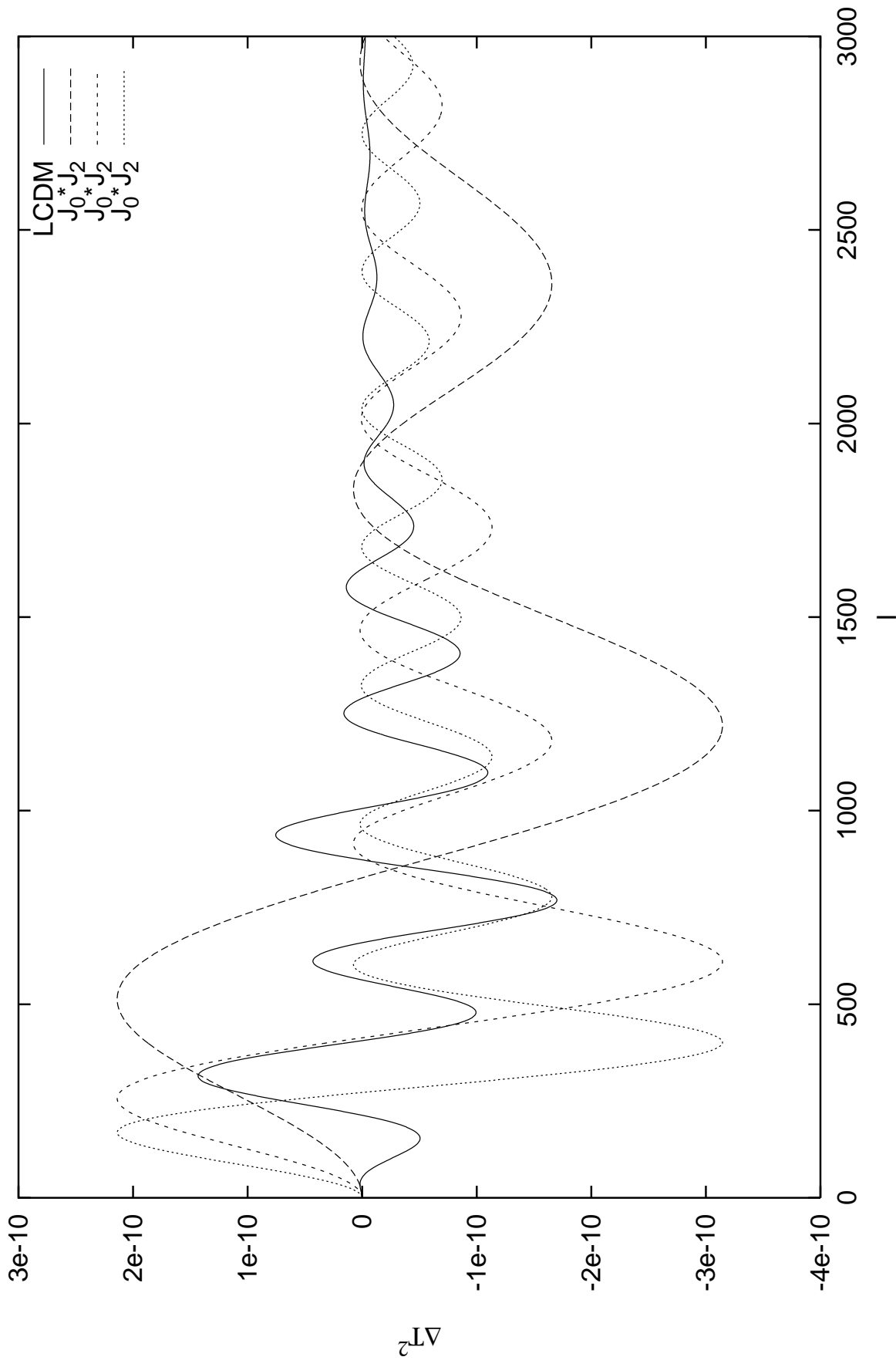


Fig. 5b

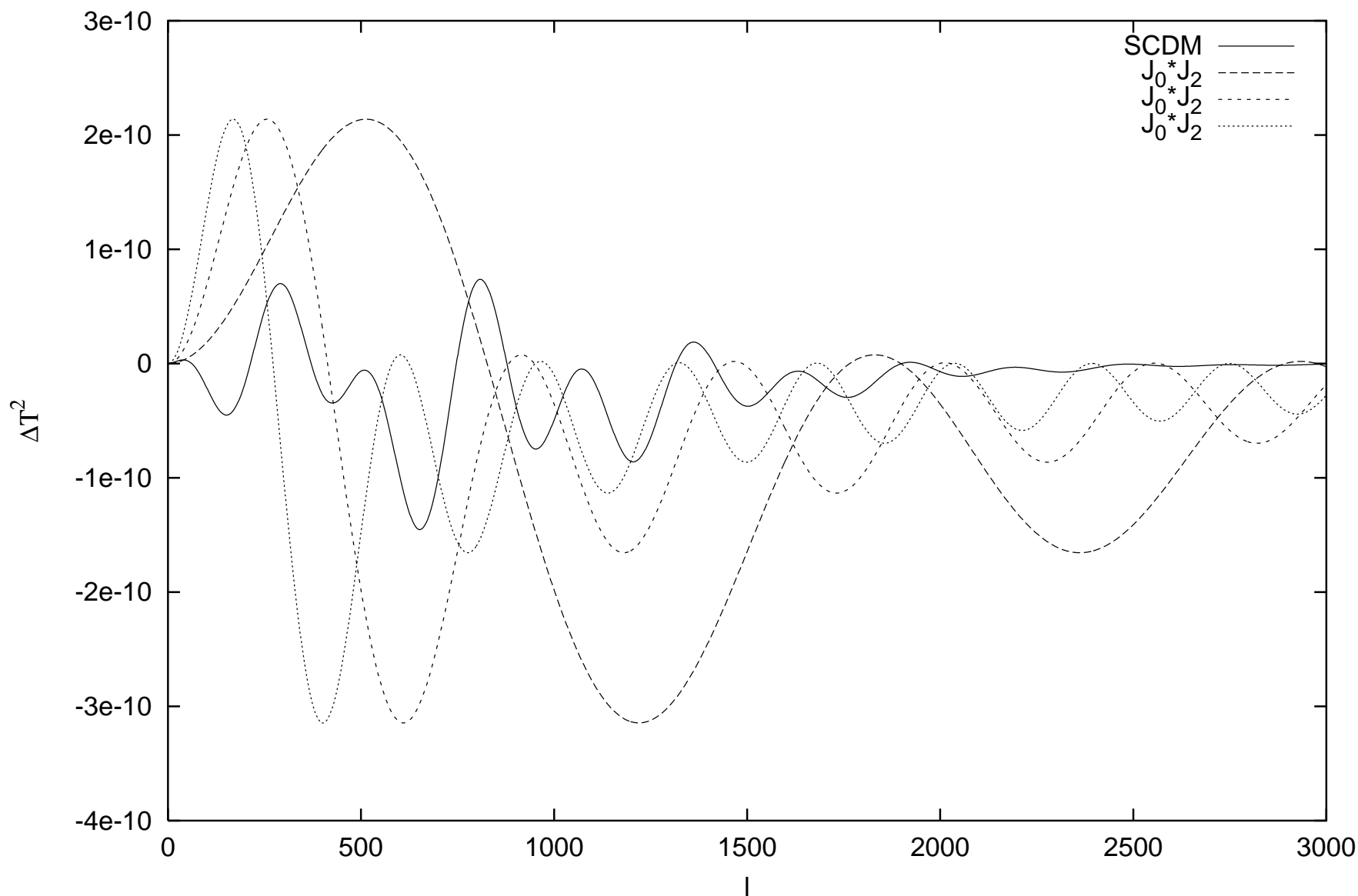


Fig. 5c

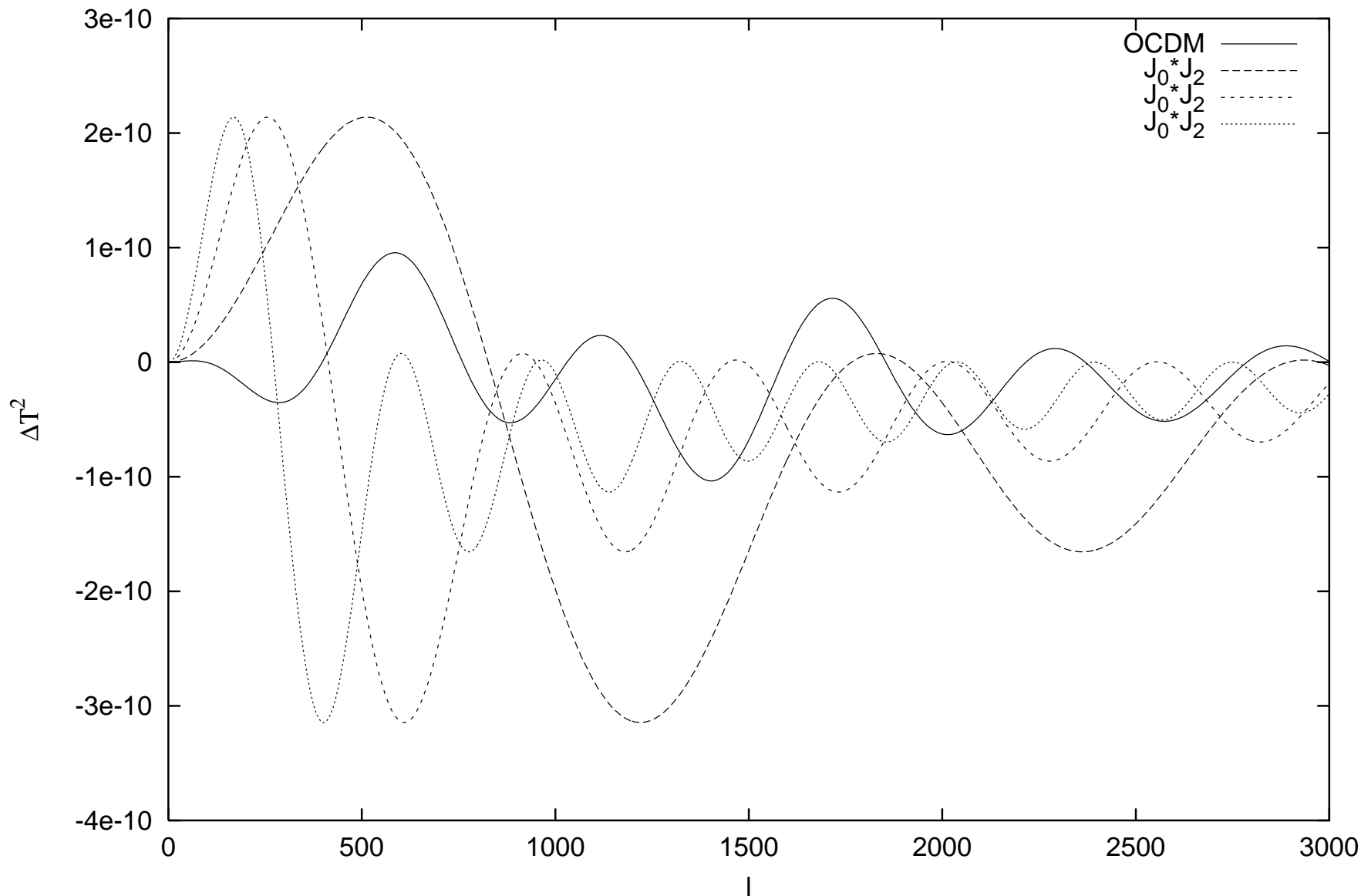


Fig. 6

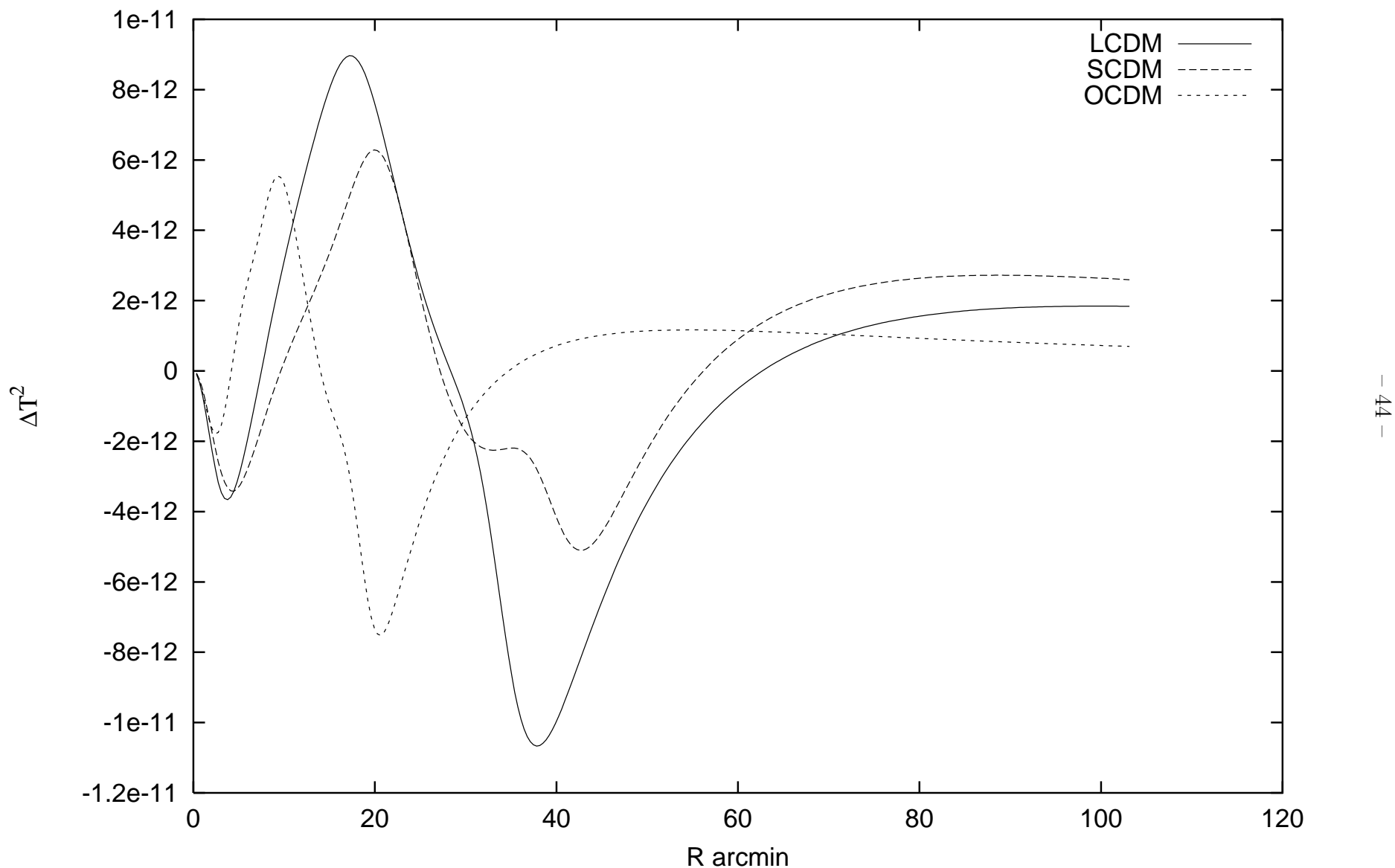


Fig. 7

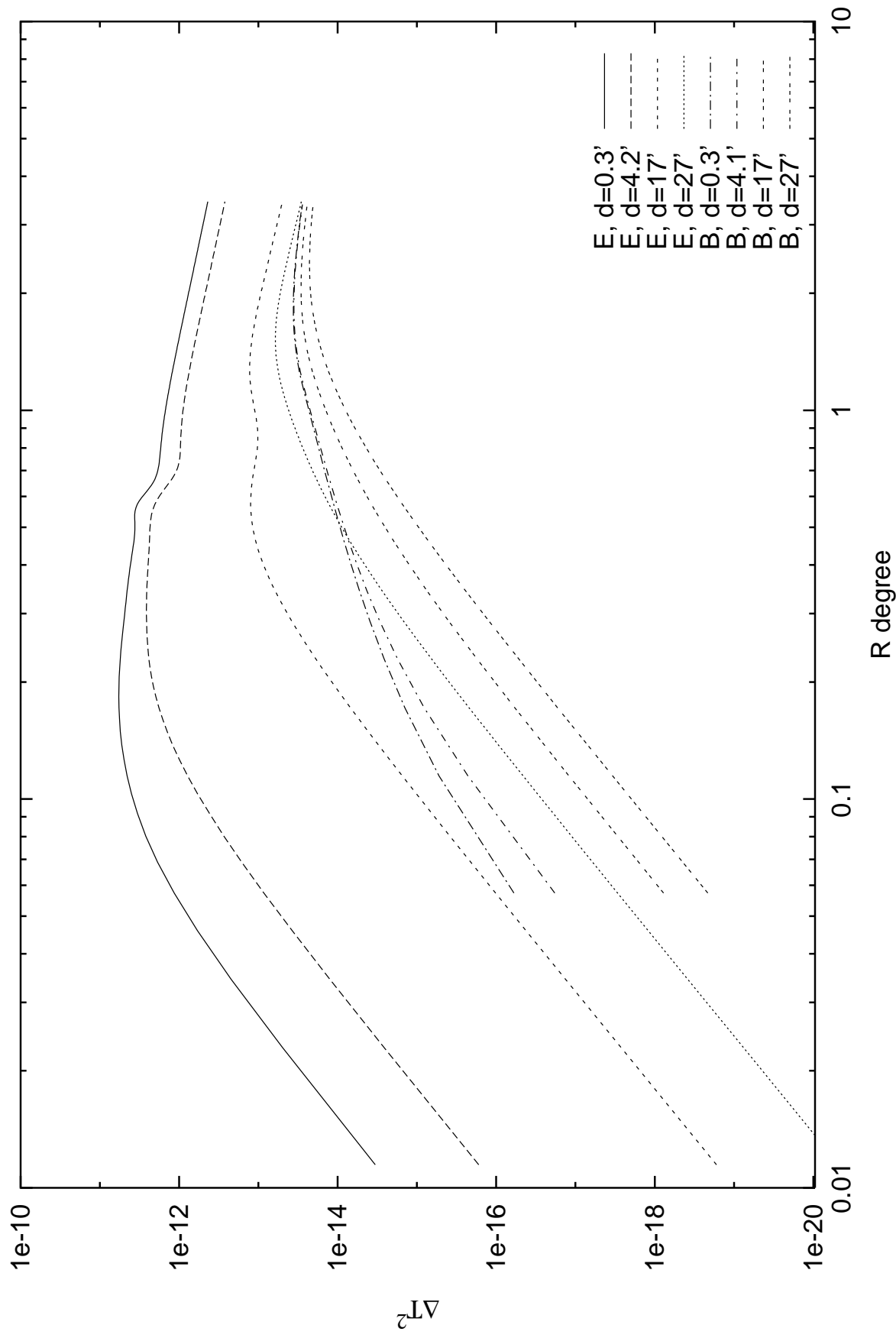


Fig 8

